Bioactive Materials 40 (2024) 148–167

Contents lists available at ScienceDirect

Bioactive Materials

journal homepage: www.keaipublishing.com/en/journals/bioactive-materials

Initial therapeutic evidence of a borosilicate bioactive glass (BSG) and Fe_3O_4 magnetic nanoparticle scaffold on implant-associated *Staphylococcal aureus* bone infection

Ying Jin [a,1], Hang Liu [a,1], Lei Chu [a,1], Jin Yang [b], Xiuyang Li [a,c], Hang Zhou [a], Haitao Jiang [a], Lei Shi [a], Jason Weeks [d], Joshua Rainbolt [d], Changjiang Yang [e], Thomas Xue [d], Haobo Pan [e], Zhongliang Deng [a,2], Chao Xie [d], Xu Cui [e,**,2], Youliang Ren [a,*,2]

[a] Department of Orthopaedics, Second Affiliated Hospital of Chongqing Medical University, 76 Linjiang Road, Yuzhong Distinct, Chongqing, 400010, PR China
[b] Department of Orthopaedics, Zunyi Medical University, Zunyi, Guizhou, PR China
[c] Department of Orthopedics, The Seventh People's Hospital of Chongqing, The Central Hospital Affiliated to Chongqing University of Technology, Chongqing, 400054, PR China
[d] Center for Musculoskeletal Research, Department of Orthopaedics & Physical Performance Center, University of Rochester Medical Center, Rochester, NY 14642, USA
[e] Shenzhen Key Laboratory of Marine Biomedical Materials, CAS-HK Joint Lab of Biomaterials, The Key Laboratory of Biomedical Imaging Science and System, Shenzhen Institute of Advanced Technology, Chinese Academy of Sciences, Shenzhen, 518055, PR China

ARTICLE INFO

Keywords:
Osteomyelitis
Staphylococcus aureus
Biofilm
Borosilicate bioactive glass
Magnetic nanoparticles

ABSTRACT

Implant-associated *Staphylococcus aureus* (*S. aureus*) osteomyelitis is a severe challenge in orthopedics. While antibiotic-loaded bone cement is a standardized therapeutic approach for *S. aureus* osteomyelitis, it falls short in eradicating Staphylococcus abscess communities (SACs) and bacteria within osteocyte-lacuna canalicular network (OLCN) and repairing bone defects. To address limitations, we developed a borosilicate bioactive glass (BSG) combined with ferroferric oxide (Fe_3O_4) magnetic scaffold to enhance antibacterial efficacy and bone repair capabilities. We conducted comprehensive assessments of the osteoinductive, immunomodulatory, antibacterial properties, and thermal response of this scaffold, with or without an alternating magnetic field (AMF). Utilizing a well-established implant-related *S. aureus* tibial infection rabbit model, we evaluated its antibacterial performance *in vivo*. RNA transcriptome sequencing demonstrated that BSG + 5%Fe_3O_4 enhanced the immune response to bacteria and promoted osteogenic differentiation and mineralization of MSCs. Notably, BSG + 5% Fe_3O_4 upregulated gene expression of NOD-like receptor and TNF pathway in MSCs, alongside increased the expression of osteogenic factors (RUNX2, ALP and OCN) *in vitro*. Flow cytometry on macrophage exhibited a polarization effect towards M2, accompanied by upregulation of anti-inflammatory genes (TGF-β1 and IL-1Ra) and downregulation of pro-inflammatory genes (IL-6 and IL-1β) among macrophages. *In vivo* CT imaging revealed the absence of osteolysis and periosteal response in rabbits treated with BSG + 5%Fe_3O_4 + AMF at 42 days. Histological analysis indicated complete controls of SACs and bacteria within OLCN by day 42, along with new bone formation, signifying effective control of *S. aureus* osteomyelitis. Further investigations will focus on the *in vivo* biosafety and biological mechanism of this scaffold within infectious microenvironment.

Peer review under responsibility of KeAi Communications Co., Ltd.
* Corresponding author.
** Corresponding author. Shenzhen Key Laboratory of Marine Biomedical Materials, CAS-HK Joint Lab of Biomaterials, The Key Laboratory of Biomedical Imaging Science and System, Shenzhen Institute of Advanced Technology, Chinese Academy of Sciences, Shenzhen, 518055, PR China.
E-mail addresses: xu.cui@siat.ac.cn (X. Cui), 306019@hospital.cqmu.edu.cn (Y. Ren).
[1] Drs. Ying Jin, Hang Liu and Lei Chu contributed equally to this article as co-first authors.
[2] Drs. Youliang Ren, Xu Cui, Zhongliang Deng contributed equally to this study as co-corresponding authors.

https://doi.org/10.1016/j.bioactmat.2024.05.040
Received 24 February 2024; Received in revised form 14 May 2024; Accepted 27 May 2024
Available online 8 June 2024

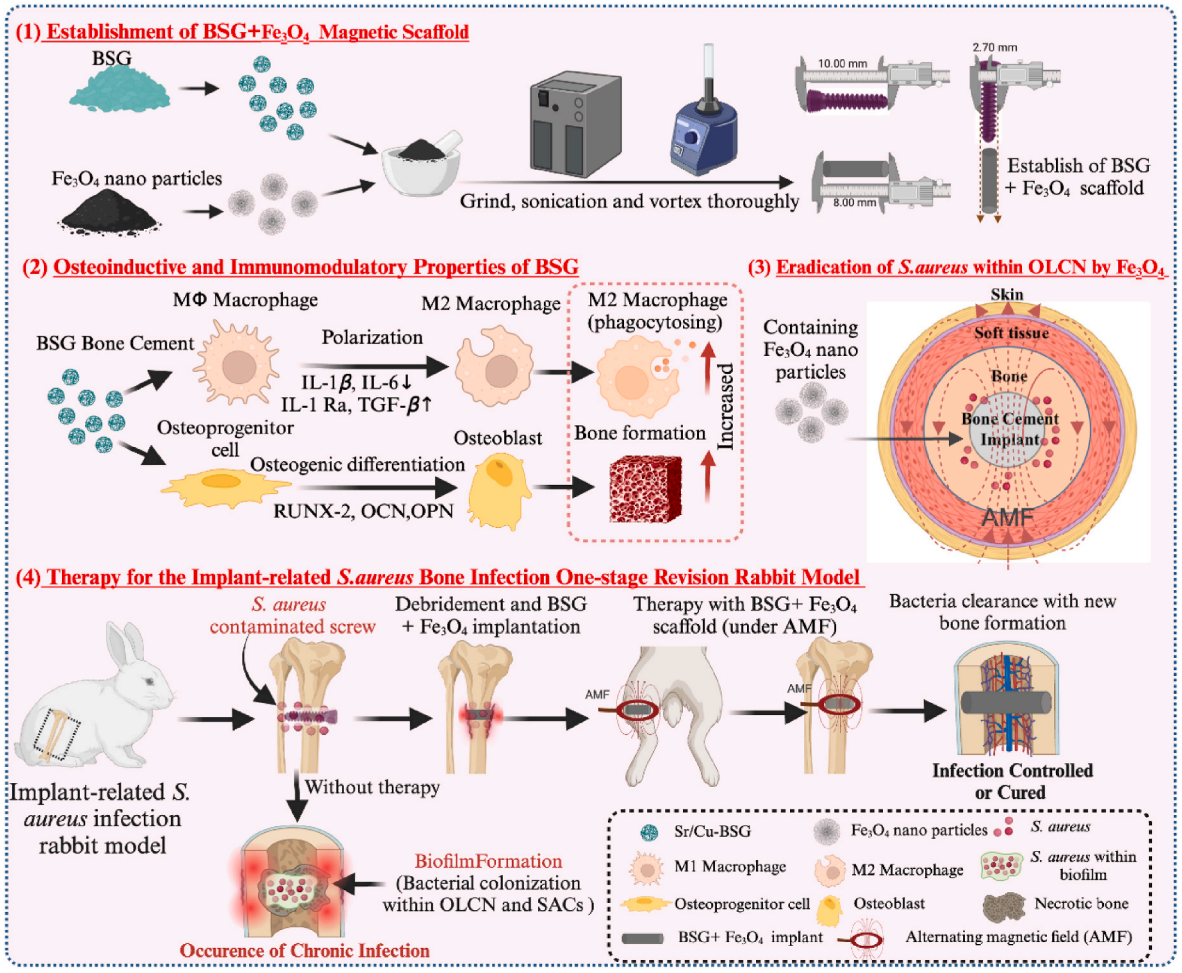

Fig. 1. A Schematic diagram of a model for the treatment of *S. aureus* related bone infection model with BSG + Fe_3O_4 magnetic scaffold. (1) To match the size of titanlnium alloy screws used for the establishment of *S. aureus* bone infection model, the size of BSG + Fe_3O_4 scaffold was prepared under the premise of full mixing. (2) BSG can promote the autoimmune regulation of M2 macrophage polarization and the bone-inducing properties of promoting osteogenesis. (3) Fe_3O_4 magnetic particles can eradicate *S. aureus* within OLCN when exposed to an AMF. (4) Establishment of an implant-related *S. aureus* bone infection model of rabbit and treatment process. In the untreated group, the infected screws were removed after challenged with *S. aureus* contaminated screw by day 7, only debridement was performed without scaffolds, as bacteria invasion and biofilm formation, the acute bone infections turned into chronic bone infections eventually. While, the treatment group suffered from debridement and implanted with BSG + Fe_3O_4 scaffolds at the original infection site, then the treatment last until 42 days under the AMF.

1. Introduction

Bone infection represents a severe complication of orthopedics, often characterized by its challenging treatment, frequent recurrent, and prolonged therapy. Across all orthopedic subspecialties, the incidence of infection ranges from 0.1% to 3%, with treatment cost of per patient estimated at approximately $17 000 to $150000 [1]. Based on our prior clinical epidemiological research *Staphylococcus aureus* (*S. aureus*) emerges as the predominant pathogen responsible for bone infections [2], and even after 29 years of treatment, recurrence of *S. aureus* bone infection persists [3,4]. Consequently, addressing *S. aureus* bone infection remains a significant clinical challenge.

Recent research has highlighted the primary cause behind the recurrence of *S. aureus* bone infections: the presence of various forms of biofilms, such as Staphylococcus abscess communities (SACs) and bacteria colonize within osteocyte-lacuna canalicular network (OLCN) [5–9]. While conventional treatment methods like debridement, irrigation, and systematic antibiotic treatment are effective against planktonic bacteria, our previous studies have shown their inefficacy against bacteria within SACs and OLCN [5,10]. Antibiotics loaded bone cement has been a staple in clinical treatment of infected bone defects since the 1960s and is widely regarded as a standard strategy [11,12]. However, recent expert consensus on antibiotic bone cement has underscored its limitations, including: its inability to fully control biofilm-associated bacteria, failure to repair bone defect, and the necessity for secondary surgery due to its non-degradability. Consequently, alternative approaches to antibiotic bone cement have garnered significant attention from researchers [12,13].

Iron oxide nanoparticles (IONPs) have gained FDA approval and stand as the most extensively researched materials in the realm of nanomedicine [14–18]. Our prior studies have validated that the efficacy of traditional ferroferric oxide (Fe_3O_4) magnetic particle bone cement under alternating magnetic field (AMF), demonstrating commendable biomechanical properties and biosafety. The cement has shown the capability to eliminate colonized *S. aureus* within OLCN, while simultaneously mitigating osteolysis resulting from bacterial infection around the affected area. However, a major drawback of this Fe_3O_4 magnetic particle bone cement lies in its non-degradability, necessitating subsequent surgical intervention [19].

With its remarkable properties for repairing both soft and hard tissue repair, borosilicate bioactive glass (BSG) has emerged as a focal point in tissue engineering research. Among the various types of bioactive glass,

silicate bioactive glass (45S5) pioneered by Professor Hench and colleagues, stands as the most extensively utilized and studied variant [20]. This bioactive glass has garnered approval from the U.S. FDA for treating bone infections. BSG represents a novel iteration of bioactive glass, integrating boron into the traditional silicate bioactive glass network [21]. The incorporation of boron diminishes network connectivity, thereby enhancing chemical reactivity and expediting glass degradation and matrix ions release. Consequently, by manipulating the boron/silicon ratio within the glass network structure and incorporating additional constituents, the degradation rate and microenvironment formation of BSG can be modulated both *in vitro* and *in vivo*. This allows for better alignment with the target tissue's microenvironment.

Recently, BSG has gained widespread traction in research concerning bone tissue repair and reconstruction across various areas such as osteomyelitis, femoral condyle defect, skull defect and femoral head necrosis [21]. Previous studies had substantiated that the magnetic polymer scaffold 5Sr3Cu-BSG exhibited exceptional abilities in promoting the expression of RUNX2 and OCN, regulating inflammatory cytokine expression to polarize macrophages towards the M2 phenotype, and ultimately degrading to facilitate bone defect repair [22]. Furthermore, studies have explored the combination of Fe_3O_4 scaffolds with BSG for bone defect repair, demonstrating that such scaffolds can enhance the expression of osteogenic factors like OPN and OCN, leading to the repair of large size bone defects [23]. However, it's worth noting that the scaffold utilized in this study lacks the mechanical support properties of bone cement. Additionally, while the antibacterial effect on *S. aureus* was investigated *in vitro*, its efficacy *in vivo*, particularly in an *S. aureus* bone infection model, remains unexplored.

We aim to introduce a novel biomaterial to address infectious bone defects, offering a solution that not only control SACs and bacteria within OLCN, but also repair infected bone defects successfully. Based on the bactericidal properties of Fe_3O_4 magnetic nanoparticles in AMF [24], taking the excellent osteoinductive and immunomodulatory properties of BSG together. Here, we develop a BSG + Fe_3O_4 magnetic scaffold, and to explore its antibacterial activity and osteogenic properties in the context of *S. aureus* bone infection *in vivo* and *in vitro* (as illustrated in Fig. 1). Through this study, we aim to introduce a novel alternative therapeutic strategy for addressing clinically refractory *S. aureus* bone infection, offering hope for improved treatment outcomes in the future.

2. Materials and methods

2.1. Fabrication and characterization of BSG + Fe_3O_4 magnetic scaffold

As described in our previous publications [19,24], a commercially available Fe_3O_4 magnetic nano particles (Lot# CAS:1317 1317-61-9, Chengdu AikeDa Chemical Reagent Co Co., LtdLtd., China) was utilized in this study. $6Na_2O{\cdot}8K_2O{\cdot}8MgO{\cdot}3SrO{\cdot}18CaO{\cdot}5SiO_2{\cdot}50B_2O_3{\cdot}2P_2O_5$ (abbreviated as 3B3Sr) were produced using a standard melt quenching method. Briefly, the desired concentrations of H_3BO_3, $CaCO_3$, SiO_2, Na_2CO_3, $SrCO_3$, $4MgCO_3{\cdot}Mg(OH)_2{\cdot}5H_2O$, K_2CO_3 and $NaH_2PO_4{\cdot}2H_2O$ (Sinopharm Chemical Co., Ltd.) were mixed well and heated in a platinum/rhodium crucible in a muffle furnace for 120 min at 1150 °C. Next, the glass melt was poured into the ice slurry, which cooled the glass melt into the glass raw material. Finally, the glass raw material was crushed, grounded and sieved through an anti-oxidation steel screen to obtain a fine powder with an average diameter of less than 40 μm. The composition of 3B3Sr glass particles was measured using inductively coupled plasma atomic emission spectrometry (ICP-OES, Optima 7000DV, PerkinElmer, Waltham, USA). 5 mg of 3B3Sr glass particles were incubated in 25 mL aqua regia in an autoclave with an environmental temperature of 190 °C and an atmospheric pressure of 20 MPa to make the standard solution for ICP-OES testing. After treatment for 10 h to achieve complete dissolution, the ion concentrations were measured from the standard solution. The setting liquid was dissolved by citric acid, chitosan (CS; deacetylation degree≥95 %), and glucose (China Aladdin Biochemical Technology Co., Ltd.) and deionized (DI) water in a weight ratio of 5:1:10:30, respectively. First, citric acid was dissolved in DI water. The CS powder was then dissolved in the acidic solution and stirred magnetically for about 30 min to obtain a clear and transparent CS solution. Glucose was then added, the solution was stirred continuously for 1 h, and the resulting coagulant solution was stored at 4 °C for future use [22].

BSG + Fe_3O_4 magnetic scaffold was mixed and cured from a solid phase with setting liquid in a solid to liquid ratio of 0.1 g: 60 μL. The solid phase was mixed by different ratios of melt derived BSG with a specific composition of 3B3Sr and commercially available Fe_3O_4 magnetic nanoparticles with size of 20–50 nm (batch CAS: 1317-61-9, Chengdu Alekta Chemical Reagent Co., Ltd., China) according to the methods used in the previous study [19,25].

3B3Sr glass particles and Fe_3O_4 magnetic nanoparticles were mixed with coagulant solution, placed in Eppendorf tubes (volume: 5 mL), evenly distributed with a vortex mixer (Vortex.Genie2T, Scientific Industries, Ltd, U.S.A.) at 3000 rpm for 30 s, and then mixed with curing liquid [23]. The mixture was then injected into a cylindrical module with dimensions of 8.0 mm and 2.7 mm in inner diameter, reference as the size of titanium screws (10.0 mm × 2.7 mm) to make a standard size cylindrical BSG + Fe_3O_4 magnetic scaffold with a load of 0%Fe_3O_4, 4% Fe_3O_4, 5%Fe_3O_4, 6%Fe_3O_4. These scaffolds with varying Fe_3O_4 concentrations respectively denoted as BSG, BSG+4%Fe_3O_4, BSG+5%Fe_3O_4 and BSG+6%Fe_3O_4, based on the percentage of Fe_3O_4 magnetic nanoparticles in the BSG matrix.

The surface morphologies of BSG + Fe_3O_4 scaffolds were characterized by FE-SEM (Field emission scanning electron microscope; Nova Nano SEM 450, FEI, Netherlands) [26]. XRD (x-ray diffraction; D8 ADVANCE A25X, Bruker, Germany) and FTIR (Fourier Transform Infrared; EQUINOXSS/HYPERION2000, BRUKER, Germany) Spectrometer were employed to analyze the phase and structure of the BSG + Fe_3O_4 scaffolds. XRD measurements conditions were conducted with Cu Kα radiation (λ = 0.15406 nm) at a scanning rate of 10°/min within the of 10–80° 2 θ range. FTIR was performed over the wavenumber range of 400–4000 cm^{-1} at a scan rate of 0.04 cm^{-1}. Additionally, the compressive strength of cured BSG + Fe_3O_4 magnetic scaffold samples were tested using a universal mechanical testing machine (ZQ-990LA) with a descending velocity of 1.0 mm/min. Three samples from each group were tested, and the results are presented as a mean ± SD.

2.2. Biomineralization and ion release of BSG + Fe_3O_4 magnetic scaffold in vitro

Cylindrical-shaped scaffolds were placed in sterile polyethylene bottles containing 7.93 mL phosphate buffer saline (PBS) (volume based on scaffold size and calculated based on reference [26]) for *in vitro* biomineralization and ion release testing. The scaffolds were immersed in PBS for 1, 3, 5, 7, 10, 14, 21, and 28 days, with PBS changed every 2 days. BSG + Fe_3O_4 scaffolds were then removed from the PBS, and the release of BO_3^{3-}, SiO_3^{2-}, Ca^{2+}, Sr^{2+}, and Fe^{3+} in the PBS was measured using ICP-OES. The pH of the PBS was measured after the BSG + Fe_3O_4 scaffolds were soaked for 7, 14, and 28 days without replacement of the PBS using a pH meter (SI series pH meter, SI600, Sentron Europe B.V.). XRD and FTIR analyses were conducted to evaluate biomineralization *in vitro*.

2.3. In vitro response of mesenchymal stem cells (MSCs) and RAW264.7 cells to BSG + Fe_3O_4 magnetic scaffold extracts

2.3.1. Cell culture and preparation of BSG + Fe_3O_4 magnetic scaffold extracts

MSCs employed in this study were mouse embryo-derived mesenchymal stem cells (C3H10T1/2), C3H10T1/2 (CCL-226) was purchased from the American Type Culture Collection (ATCC, Manassas, VA).

RAW264.7 cells, mouse mononuclear macrophage leukemia cells, were purchased from Wuhan Pricella Biotechnology Co., Ltd. (China). The cell lines were cultured in Dulbecco's Modified Eagle Medium (DMEM, Gibco, USA) and Roswell Park Memorial Institute 1640 Medium (RPMI 1640, Gibco, USA), respectively, supplemented with 10 % (v/v) fetal bovine serum (FBS, Gibco, USA) and 1 % (v/v) penicillin-streptomycin (PS, Beyotime, China). Culturing was conducted in an incubator (Thermo, USA) under standard conditions, 37 °C and 5 % CO_2. When cell confluency reached approximately 80 %, passaging was performed using 0.25 % trypsin (Beyotime, China), and passage numbers 6–8 were utilized for the experimental procedures.

BSG + Fe_3O_4 magnetic scaffolds were submerged in DMEM, RPMI 1640 and osteogenic induction medium (OIM, containing ascorbic acid 50 nM, dexamethasone 0.1 μM, and β-glycerophosphate 10 mM) at a ratio of 0.1 mg/ml (sample weight to medium volume) following the previous established protocols [22]. The immersed samples were subjected to constant shaking (60 rpm, Blue pard, China) at 37 °C for 24 h to obtain the BSG + Fe_3O_4 magnetic scaffold extract medium. The extract medium was then centrifuged at 1000 rpm for 5 min (Thermo Fisher, Germany) and syringed through a 0.22 micron-rated filter. Finally, extracts were gradient diluted by a factor of 2 for future use.

2.3.2. Effect of BSG + Fe_3O_4 magnetic scaffold extract on cytotoxicity, proliferation, viability, and cytoskeleton of MSCs

MSCs were seeded in 96-well plates, in medium (100 μL/well) for 24 h, the medium was displaced with scaffold extract DMEM diluted 0-, 2-, 4-, 8-, 16-, 32-, 64-, 128- and 256-fold (diluted with DMEM and containing 10 % FBS), cells were also cultured in DMEM without extracts as a blank control. After 1 day, the DMEM was removed, and cells were treated with new DMEM containing 10 % CCK8 working solution (100 μL/well), cultured away from light for 2 h, and then the absorbance was measured with a Multiskan Spectrum Microplate Spectraphotometer (Thermo, USA) at a wavelength of 450 nm to detect the cell viability.

To assess MSCs proliferation, a CCK8 assay was employed. MSCs were seeded in 96-well plates and allowed to adhere for 24 h. Subsequently, they were cultured in scaffold extract DMEM (100 μL/well), which were diluted 32-, 64-, 128- and 256-fold or in blank medium. After incubating for 1 day, cell proliferation was detected by the CCK8 assay using the same methodology as previously described. Futhermore, MSCs were evenly seeded in confocal dishes, after 24 h, the medium was displaced with scaffold extract DMEM diluted 128-fold or in blank DMEM. And after 2 days of culture, the cells were stained with Beyo-Click™ EdU Cell Proliferation Kit with Alexa Fluor 594 (C0078S, Beyotime, Shanghai, China) to observe the cell proliferation under a confocal microscope.

Cell viability was assessed utilizing a Calcein/PI assay. MSCs were evenly seeded in confocal dishes for 24 h, and then cultured with a 128-fold dilution of scaffold extracts or medium alone. Following this, the cells were stained with the Calcein/PI Cell Viability Cytotoxicity Assay Kit (C2015 M, Beyotime, Shanghai, China) to measure cell viability after incubated at 37 °C for 30 min in the absence of light. Additionally, the nucleus and actin cytoskeleton were visualized by staining with DAPI and Actin-Tracker Red-594 to observe cell morphology.

Table 1
Primers used for RT-qPCR analysis.

Gene	Forward primer (5′–3′)	Reverse primer (5′–3′)
β-actin	CCACCATGTACCCAGGCATT	CGGACTCATCGTACTCCTGC
RUNX2	GCCGGGAATGATGAGAACTA	GGACCGTCCACTGTCACTTT
ALP	TAACACCAACGCTCAGGTCC	TGGATGTGACCTCATTGCCC
OCN	AAGCAGGAGGGCAATAAGGT	TAGGGCAGCACAGGTCCTAA
TGF-β1	CAGTACAGCAAGGTCCTTGC	ACGTAGTAGACGATGGGCAG
IL-1Ra	CTCCAGCTGGAGGAAGTTAAC	CTGACTCAAAGCTGGTGGTG
IL-6	CTTGGGACTGATGCTGGTGA	TTGGGAGTGGTATCCTCTGTGA
IL-1β	TGGAGAGTGTGGATCCCAAG	GGTGCTGATGTACCAGTTGG

2.3.3. RNA transcriptome sequencing

MSCs were evenly seeded in a 6-well plate. At ~80 % confluency, the cell culture medium was replaced by scaffold extract OIM (2 mL/well) diluted 128-fold. Cells were cultured in OIM without scaffold extracts as a negative control. After 7 days of incubation, cells were washed twice with PBS, total RNAs of the samples were isolated and purified using TRIzol (Invitrogen, CA, USA) according to the manufacturer's protocol. Agarose gel electrophoresis was used for analysis of RNA integrity and presence of DNA contamination. NanoDrop ND-1000 (Wilmington, DE, USA) was performed for detection of RNA purity (OD260/280 and OD260/230 Ratio). Agilent Bioanalyzer 2100 (Agilent, CA, USA) detected RNA integrity. RNA purification, reverse transcription, library construction and sequencing were performed by Guangzhou IGE Biotechnology (Guangzhou, China).

For RNA sample preparations, 1 μg of RNA per sample was utilized as input material. Sequencing libraries were generated using NEBNext® UltraTM RNA Library Prep Kit for Illumina® (CatalogE7530L, NEB, USA) in accordance with the manufacturer's instructions, with index codes were added to attribute sequences to each sample. Following qualification of the library test, sequencing was performed on the Illumina NovaSeqTM 6000 (IGE Biotechnology Co.,Ltd. Guangzhou, China) platform to generate 150 bp paired-end reads, according to the manufacturer's instructions.

An index of the reference genome was built using Hisat2v2.0.5 and paired-end clean reads were aligned to the reference genome. The mapped reads of each sample were assembled using StringTie with default parameters. Then, all transcripts from all samples were merged to reconstruct a comprehensive transcriptome using gffcompare software. RSEM (RNA-Seq by Expectation-Maximization) was used to count the read numbers mapped to each gene. Next, the FPKM (fragments per kilobase million) of each gene was calculated based on the length of the gene and read count mapped to it. Differential expression analysis of two conditions/groups (two biological replicates per condition) was performed using the DESeq2 R package. Gene Ontology (GO) enrichment analysis of differentially expressed genes was implemented by the cluster Profiler R package, in which gene length bias was corrected. GO terms with P value less than 0.05 were considered significantly enriched by differentially expressed genes. We used the cluster Profiler R package to test the statistical enrichment of differentially express genes in KEGG pathways.

2.3.4. Effect of BSG + Fe_3O_4 magnetic scaffold extract on osteogenic differentiation in MSCs

Alkaline phosphatase (ALP) activity was assessed to observe osteogenic differentiation of MSCs in response to BSG + Fe_3O_4 magnetic scaffold extracts. Initially, the cells were seeded in 24-well plates and cultured in OIM (1 mL/well). After 24 h, the medium was replaced with scaffold extract OIM (1 mL/well) diluted 32-, 64-, 128- and 256-fold. After 7 days of incubation, the cells were washed twice with PBS and then stained with BCIP/NBT Alkaline Phosphatase Color Development kit (C3206, Beyotime, Shanghai, China). Briefly, the staining solution contained ALP buffer, BCIP, and NTB in a ratio of 10 mL: 33 μL: 66 μL. 200 μL of staining solution was added to each well and stained in the dark for 15 min. Following staining, the plates were dried and photographed using a fluorescence microscope (Nikon, Japan). Quantitative analysis was performed using ImageJ.

Alizarin Red S staining was employed to assess late matrix mineralization of MSCs in response to BSG + Fe_3O_4 magnetic scaffolds. The cells culture method mirrored that of ALP staining. After 21 days of incubation, the medium was aspirated, and the MSCs were washed twice with PBS and fixed with 4 % paraformaldehyde for 10 min. After fixation, the cells were gently rinsed with PBS at pH 4.2 and then developed with a prepared 0.4 % Alizarin Red S solution to visualize calcium deposition indicative of late-stage osteogenesis. Finally, the plate was scanned using a fluorescence microscope, and quantitative analysis was performed.

RNA isolation, cDNA preparation, and real-time quantitative polymerase chain reaction (RT-qPCR) analysis were performed on MSCs exposed to scaffold extracts. Cells were pre-seeded in 6-well plates, and cultured with scaffold extract OIM (2 mL/well) diluted 128-fold after adhesion. After 7 or 14 days of incubation, total RNA was extracted using the RNA Quick Purification Kit (Shanghai Yishan Biotech, China). Subsequently, the RNA was reverse-transcribed to cDNA using the PrimeScript™ RT reagent Kit (Takara, Japan). The resultant cDNA was then diluted 5- to 10-fold for the RT-qPCR assay. The expression levels of the target genes, including RUNX2, ALP, and OCN, were assessed using β-actin as the housekeeping gene for normalization. The primer sequences used in this study are shown in Table 1 [27,28].

Protein extraction from MSCs exposed to scaffold extracts was performed followed by Western blot analysis. The cells were cultured according to the same protocol as described previously. At the designated timepoint, cells were washed twice with cold PBS (4 °C) and 300 μL of RIPA Lysis Buffer (P0013B, Beyotime, China) was added to each well, and the cells was incubated on ice for 30 min. Subsequently, the lysed cells were transferred into 1.5 ml centrifuge tubes, these tubes were then bathed in boiling water for 10 min with the addition of 75 μL Omni-Easy™ Instant Protein Sample Loading Buffer (EpiZyme, China) and 15 μL β-mercaptoethanol (Gibco, USA) in each tube.

Protein samples were separated by sodium dodecyl sulfate polyacrylamide gel electrophoresis, and then the target gels were transferred to polyvinylidene difluoride (PVDF) membranes. The membranes were soaked in Protein Free Rapid Blocking Buffer (PS108P, EpiZyme, China) for 15 min at room temperature and then incubated in the corresponding primary antibody solutions at 4 °C overnight. The membranes were washed four times using Tris-buffered saline Tween20 (TBST) and incubated in corresponding biotin-labeled immunoglobulin G (IgG, Beyotime, China) for 0.5 h at room temperature. Next, the membranes were washed four times using TBST and incubated in horse radish peroxidase (HRP)-labeled streptavidin (Beyotime, China) for 0.5 h at room temperature. Then the membranes were washed four times by TBST. Finally, the images of the target bands on the membranes were developed using *Tanon*-5200 (shanghai, China). The antibodies were diluted in QuickBlock™ Western Primary Antibody Dilution (P0256, Beyotime, China) according to the instructions (1:1000), the biotin-labeled IgGs were diluted 1:3000 in TBST, and the HRP-labeled streptavidin was diluted 1:10000 in TBST.

2.3.5. Macrophage polarization and inflammation-related gene expression of RAW264.7 cells

The macrophage used in this study were RAW264.7 cells [22]. The cells were evenly seeded in 6-well plates and treated with scaffold extract medium (2mL/well) diluted 128-fold in RPMI 1640 for 3 days after cells attachment, and then macrophage polarization was detected by flow cytometry. Briefly, at the designed timepoint, RAW 264.7 cells were trypsinized and centrifuged at 1000 rpm for 5 min. Next, cells were resuspended in 0.5 ml of PBS, fixed with 4 % (w/v) formaldehyde at room temperature for 15 min, washed twice with PBS, and then incubated in a 1.5 ml Eppendorf tube with CD80 (M1-marked, 1:100, Biolegend, 104705) and CD206 (M2-marked, 1: 800, Biolegend, 141703) at 4 °C for 30 min. Cells were then centrifuged at 1000 rpm for 5 min, supernatant was discarded, and the cells were resuspended in PBS. The polarization states (M1/M2) of RAW 264.7 cells were analyzed using a cytoFLEX Flow Cytometer (Beckman, China) and software FlowJo X.

Gene expression levels of anti-inflammatory genes (TGF-β1 and IL-1Ra) and pro-inflammatory genes (IL-6 and IL-1β) were measured via RT-qPCR after culturing RAW 264.7 cells in BSG + Fe_3O_4 magnetic scaffold extract RPMI 1640 for 3 days. The total RNA was extracted using the RNA Quick Purification Kit (Shanghai Yishan Biotech, China), followed by reverse transcription to generate cDNA. The target genes were analyzed by RT-qPCR. The expression of the housekeeping gene β-actin was used to normalize the PCR results, and TGF-β1, IL-1Ra, IL-6 and IL-1β were the target genes. The primer sequence information is provided in Table 1.

2.4. Evaluation of the magnetothermal responsiveness of BSG + Fe_3O_4 scaffolds ex vivo

Independent samples of BSG + 4%Fe_3O_4, BSG + 5%Fe_3O_4 and BSG + 6%Fe_3O_4 were positioned within the coil of a magnetic thermal analyzer. These samples were then exposed to an AMF for 3 min. The parameters of the magnetic field were as follows: frequency of 626 kHz, output current of 28.6 A, number of coils turns of 2, coil length of 1 cm, field strength of 5.72 kA/m. During the exposure, the real-time temperature was recorded every 10 s, ranging from 0 s to 180 s. This temperature measurement was conducted using a far-infrared thermometer (FOTRIC225, ZXF Laboratories, USA). Each BSG + Fe_3O_4 material underwent three times independent tests, and the average temperature value was calculated for subsequent statistical analysis. The thermal images captured during the experiment were analyzed using AnalyzIR 7.1 (ZXF Laboratories, USA) [19].

Subsequently, the distal epiphysis of the right tibial shaft of rabbits was obtained (a 5 cm section close to the tibial plateau, including complete muscle, bone and marrow), the BSG + 5%Fe_3O_4 material was vertically inserted into the center of the bone marrow. Subsequently, the embedded implant was immediately subjected to an AMF for 180 s, during which the temperature of the scaffold was recorded every 10 s. Starting from the center of the material, five points were randomly selected in each of the four directions-up, down, left and right. The distance and temperature at each point were recorded in relation to the starting point. Scatter plots were generated in statistical software to analyze the thermal decay distance. All thermal images were analyzed using AnalyzIR 7.1.

2.5. Antibacterial circle experiment of BSG + 5%Fe_3O_4 magnetic scaffold in vitro

The polymethylmethacrylate (PMMA) liquid monomer (10 mL) comprises methyl methacrylate (9.2 g) and N, *N*-dimethyl-p-toluidine (0.2 g). The commercial PMMA powder Ostetal ® V (Heraeus Medical GmbH, Hanau, Germany), consists of PMMA (14.2 g), zirconia (11.7 g), and benzoyl peroxide (0.1 g). These components are mixed together and injected into a cylindrical module to form a standard-size PMMA cylinder.

The PMMA, BSG, and BSG + 5%Fe_3O_4 were disinfected for 58 min at low temperature using a hydrogen gas plasma sterilizer (LAOKEN LK/MJQ-100). The Mid-logarithmic-phase *S. aureus* (ATCC29213) was diluted to 1 × 10^5 CFU/mL with PBS, and 20 μL of the solution was spread on the TSA plate (diameter: 2.5 cm). Next, PMMA, BSG, and BSG + 5%Fe_3O_4 were vertically inserted into the center of the TSA plate and placed in an AMF for 180 s. Another group of BSG + 5%Fe_3O_4 was not subjected to a magnetic field and was incubated overnight at 37 °C under 5%CO_2. Images were taken by the Scan®1200-HD automated colony counter from INTERSCIENCE. Antibacterial capability was assessed by measuring the diameter of the sterile zone (clear zone) within the image. Each group contained 5 samples. The diameter of each sample measured randomly three times, and the average value was used for statistical analysis.

2.6. Establishment of implant-related S. aureus bone infection one-stage revision rabbit model

All animal experiments were approved by Second Affiliated Hospital of Chongqing Medical University. All rabbits were male New Zealand white rabbits, weighing 2–2.5 kg, aged between 12 and 14 weeks. The study was divided into untreated group, BSG + 5%Fe_3O_4 group and BSG+5%Fe_3O_4+AMF group. There are a total of 15 rabbits in each group.

For experimentation, intramuscular injection of a mixture of

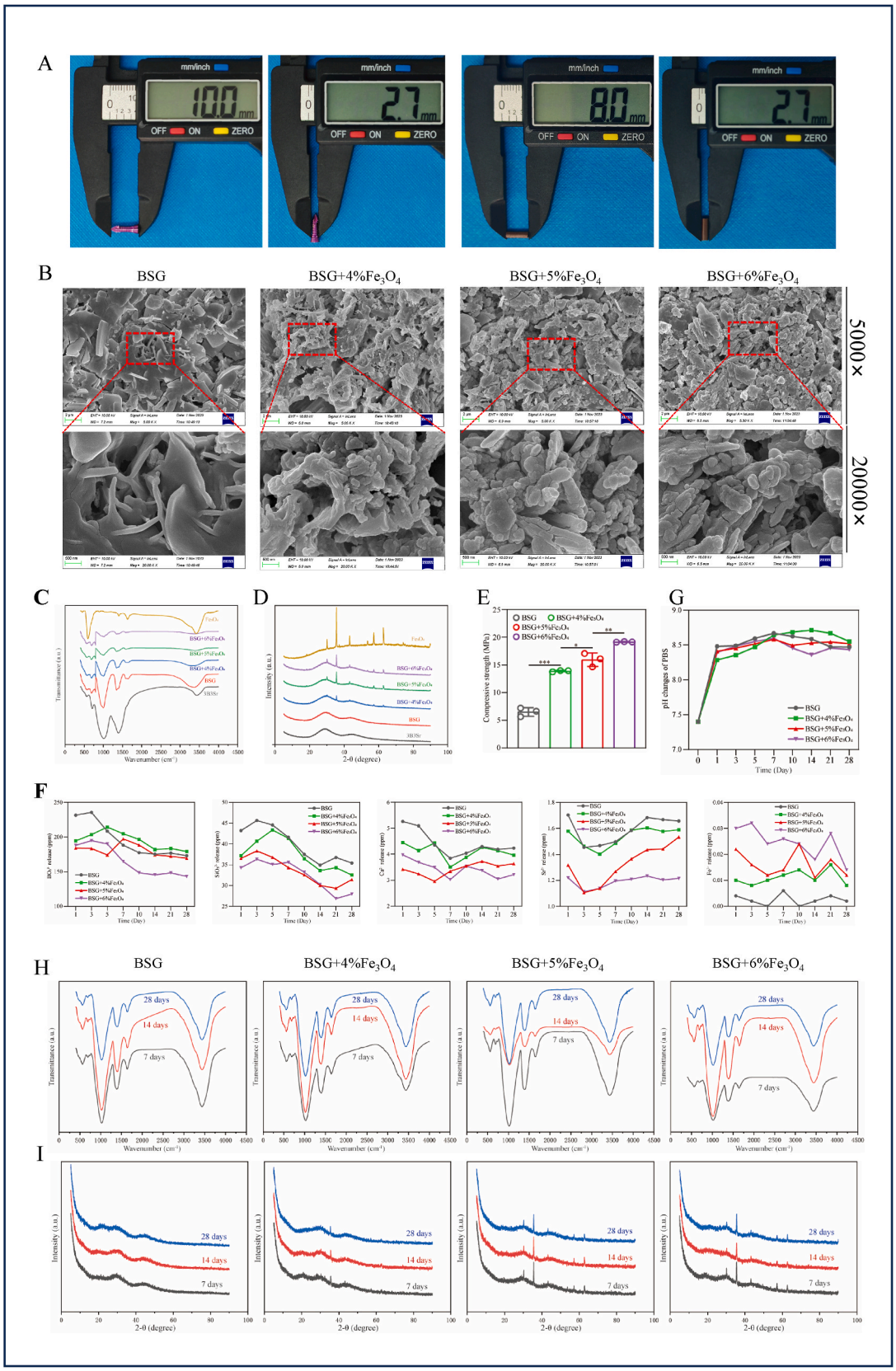

Fig. 2. Morphological characterization and biomechanical properties of BSG + Fe_3O_4 magnetic scaffold. A) BSG + Fe_3O_4 scaffolds were compounded to match the size of the titanium screws use in the *in vivo* model. B) SEM images of the microarchitecture of BSG + Fe_3O_4 magnetic scaffolds, at 5000X and 20000X magnifications. C-D) FTIR spectra and XRD patterns of 3B3Sr, BSG, Fe_3O_4, and BSG with 4%, 5%, or 6%Fe_3O_4. E) Compressive strength (MPa) of each scaffold group (n = 3), presented as mean ± SD. F) Release of ions including BO_3^{3-}, SiO_2^{2-}, Ca^{2+}, Sr^{2+} and Fe^{3+} from scaffolds incubated in PBS were quantified and plotted across multiple time points. Each data point represents the total released over two days. G) pH of PBS solution containing BSG + Fe_3O_4 scaffolds, measured to 28 days. H–I) FTIR spectra and XRD patterns of BSG + Fe_3O_4 scaffolds after immersion in PBS for 7, 14 and 28 days.

ketamine (25 mg/kg) and xylazine (1.5 mg/kg) was used for induction of anesthesia, and anesthesia was maintained with the inhalation of isoflurane. Mid-logarithmic-phase *S. aureus*, prepared into a bacterial solution of 1×10^5 CFU/mL using tryptic soy broth (TSB). Through overnight culturing, the concentration reached $4.8 \times 10^{10} \pm 2.4 \times 10^{10}$ CFU/ml, then which was used to contaminate sterile titanium screws overnight. Subsequently, the bacteria loaded titanium screws were air-dried for 30 min in a sterile laminar flow hood. By performing CFU assay, we determined that each screw loaded $8.5 \times 10^7 \pm 4.75 \times 10^7$ CFU/screw of *S. aureus* after overnight culturing. Then, those screws were them implanted into the right upper metaphysis of the rabbit tibia. The infection modeling surgery was conducted on day 7. After 1 week of breeding, rabbits were randomly divided into three groups for treatment and labeled as day 0. The experimental animals underwent the rigorous implant removal and debridement procedures, followed by immediate suturing of the incision. The BSG+5%Fe_3O_4 group had screws removed and debridement performed as the untreated control group before implanting BSG + 5%Fe_3O_4 material into the screw tract, so it was buried beneath the bone surface. The BSG + 5%Fe_3O_4 + AMF group had screws removed, debridement performed locally as the other two groups, and then BSG + 5%Fe_3O_4 material was implanted into the screw tract and buried beneath the bone surface. The rabbit's affected leg was placed in the coil of a magneto-thermal analyzer daily and treated for 180 s in a magnetic field while under anesthesia with isoflurane, until euthanasia as day 42.

Six rabbits in each group were randomly selected and euthanized to observe early and late soft tissue and bone infections near the nail path on day 7 and day 42. On day 1 and day 28, six rabbits were randomly selected from each group for euthanasia via air embolism and right tibia specimens were collected, histopathological characterization was evaluated using hematoxylin and eosin (H&E) staining and Gram staining. Three rabbits were randomly selected from each group and underwent computed tomography (CT) under isoflurane anesthesia on days 7, 14, 28 and 42. After scanning on day 42, they were euthanized, and histopathological features were evaluated using H&E staining and Gram staining.

2.7. Computed tomography (CT) analysis

On day 7, 14, 28 and 42 post-implantation, CT scans were conducted on the rabbits under isoflurane anesthesia. The scans were performed using a 320-slice CT scanner (Aquilion ONE, Canon Medical Systems, Japan), with a tube voltage of 100 kV and tube current set at 50 mA, and the scan field encompassed 220 mm. Each group consisted of three rabbits. Following the CT-scans, three-dimensional reconstruction of the acquired images was carried out with a thickness of 0.5 mm.

2.8. Histological characterization of infected tibiae

On day 1, 28 and 42 post-implantation, three rabbits from each group were euthanized via air embolism. Subsequently, right tibia specimens were collected, decalcified, and subjected to further analysis. H&E staining and Gram staining were performed to assess the histopathological features. Panoramic DESK, P-MIDI, P250 (3D HISTECH; Hungary) were used to scan images and analyze histopathological features.

2.9. Statistical analysis

In this study, the statistical analysis software used was GraphPad Prism 9.5.1, and data was analyzed by using one-way ANOVA and two-way ANOVA. All analyses of difference were presented as mean ± SD, with P value < 0.05 considered significant. For all quantitative analyses, results were replicated in at least three independent experiments.

3. Results

3.1. Morphology, compressive strength, biomineralization and ions release of BSG + Fe_3O_4 magnetic scaffold

Firstly, BSG + Fe_3O_4 compounds were fabricated into scaffolds, aligning their dimensions with those of the titanium screws employed *in vivo* (Fig. 2A). As shown in SEM (Fig. 2B), BSG particles and Fe_3O_4 nanoparticles were mixed evenly. Notably, the absence of clustered crystallization or inter-nanoparticle connection suggested successful integration of Fe_3O_4 magnetic nanoparticles into the BSG matrix without compromising its microstructure.

Further analysis through FTIR (Fig. 2C) demonstrated that all BSG + Fe_3O_4 compounds exhibited similar infrared characteristic vibration peaks to 3B3Br. The intensity of these characteristic infrared peaks tended to diminish with the increasing Fe_3O_4 content, possibly attributed to the infrared absorption effect of Fe_3O_4. Additionally, XRD results (Fig. 2D) indicated that the presence of typical "steamed bread peaks" of borosilicate glass around 30°and 45° in 3B3Br and BSG, without any additional heterogeneous peaks, indicating the amorphous structure of the glass. With increasing doping of Fe_3O_4 magnetic nanoparticles, the intensity of these characteristic peaks heightened, with BSG + 5%Fe_3O_4 magnetic scaffold exhibiting the sharpest and strongest diffraction peak consistently compared to other scaffold, indicating that Fe_3O_4 was uniformly incorporated into the bone cement. Importantly, the doped scaffolds retained their characteristic "Broad Peak", suggesting that the incorporation of different Fe_3O_4 proportions did not alter the amorphous structure of the glass.

The results (Fig. 2E) demonstrate that the compressive strength of the BSG + Fe_3O_4 magnetic scaffolds increased with escalating concentration of Fe_3O_4 nano particles. The compressive strength of BSG, BSG + 4%Fe_3O_4, BSG + 5%Fe_3O_4 and BSG + 6%Fe_3O_4 were recorded as 6.50366 ± 0.77762 MPa, 13.88051 ± 0.12054 MPa, 15.93383 ± 1.21466 MPa and 19.14661 ± 0.05417 MPa, respectively. Remarkably, the compressive strength of all Fe_3O_4 nano particle-containing BSG groups reached in our study was found to be comparable to that of human cancellous bone (2–12 MPa) [29]. This suggests the potential of BSG + Fe_3O_4 scaffolds to withstand mechanical stresses akin to natural bone tissue, enhancing their suitability for orthopedic applications.

The release profiles of BO_3^{3-}, SiO_3^{2-}, Ca^{2+}, Sr^{2+}, Fe^{3+} ions from the scaffolds, as plotted across multiple time points, exhibited significant variability (Fig. 2F). This variance could be attributed to the unique chemistry of each ion affecting its relative affinity for the compound. Notably, the percentage of Fe_3O_4 in the scaffold showed an inverse correlation with the overall quantity of ions released. This phenomenon can be contributed to a lower percentage of BSG in the compounds with higher Fe_3O_4.

The pH curve of PBS for all BSG + Fe_3O_4 groups displayed a similar trend (Fig. 2G). Initially, starting at 7.4, the pH of the PBS increased rapidly during the first 7 days of immersion, followed by a more gradual increase, ultimately reaching a plateau after 7 days. The PBS pH values after 28 days of immersion were recorded as 8.470, 8.550, 8.520 and 8.435 for BSG, BSG + 4%Fe_3O_4, BSG + 5%Fe_3O_4 and BSG + 6%Fe_3O_4, respectively. As previously reported, lower alkaline pH could potentially contribute to reducing inflammatory reactions *in vivo*, thus indicating a favorable biocompatibility profile of this BSG + Fe_3O_4 magnetic scaffolds [30].

FTIR and XRD were performed for BSG + Fe_3O_4 magnetic scaffold after immersion in PBS for 7, 14 and 21 days. As indicated in FTIR spectra results (Fig. 2H), it was observed that after immersion in PBS for 7 days, the major vibrational bands associated with BSG present in the FTIR spectra of the BSG + Fe_3O_4 magnetic scaffolds. Furthermore, a decrease in the overall absorbance of the spectra was noted with increasing immersion time, suggesting degradation of BSG without significant changes to the chemical composition. Subsequently, the structures of the BSG + Fe_3O_4 scaffolds after immersion were then

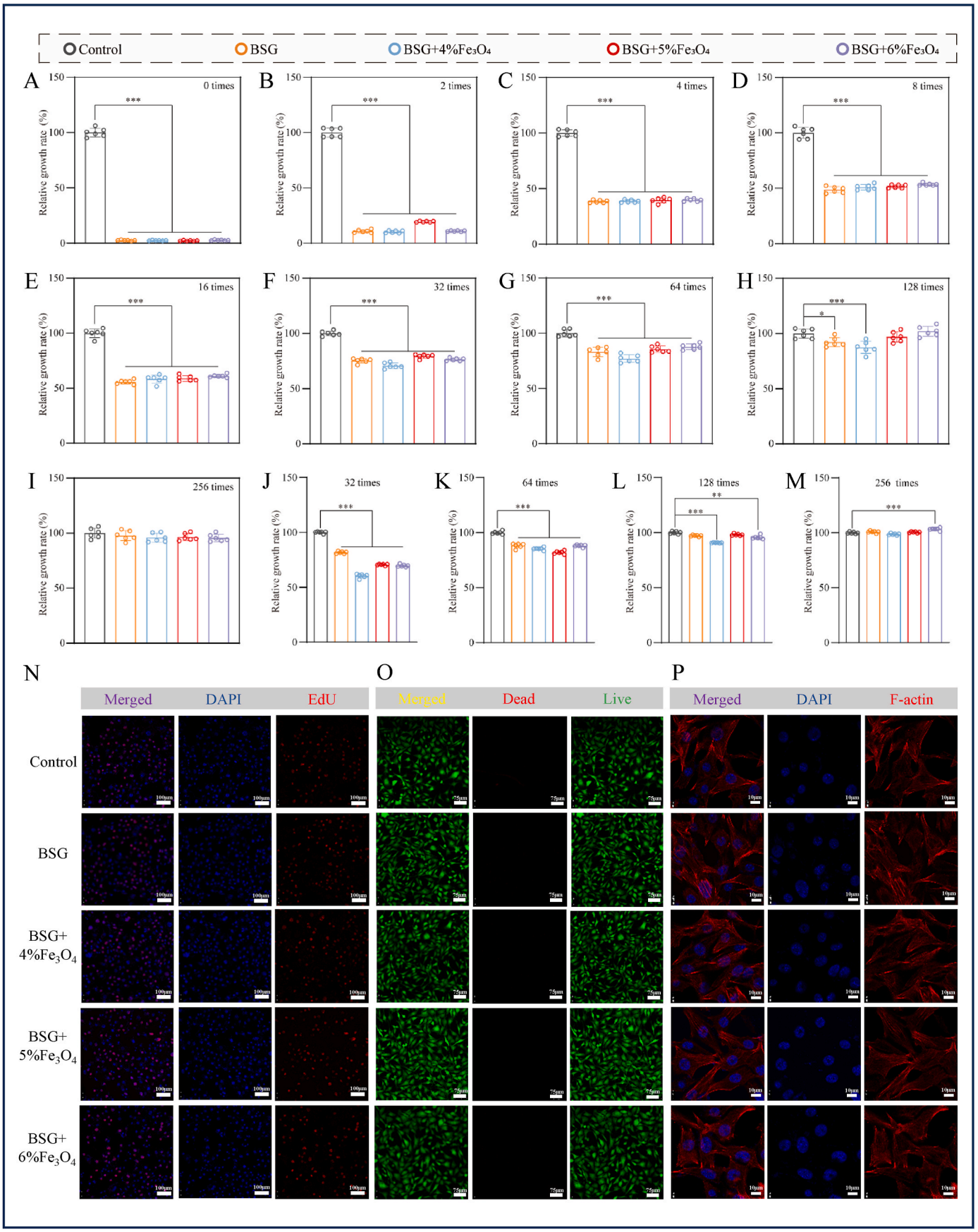

(caption on next page)

Fig. 3. Cytotoxicity, proliferation, viability, and cytoskeleton of MSCs when cultured with a 128-fold dilution of BSG + Fe_3O_4 magnetic scaffold extracts. A-I) CCK8 results were obtained after culturing cells in extracts of different concentrations of BSG + Fe_3O_4 for 1 day. Cells exhibited lower survival ratio until the extract was diluted 128 times. J-M) MSCs proliferation was assessed using CCK8 after being culturing in 32-, 64-, 128-, and 256-fold dilutions of BSG + 5%Fe_3O_4 extract for 1 day. The 128-fold dilution of BSG + 5%Fe_3O_4 extract had no impact on cell proliferation. N) EdU cell proliferation staining, O) live/dead staining, and P) cytoskeleton staining of MSCs cultured with 128-fold dilutions of the scaffold extracts for 2 days. These results indicated that the extracts of each polymer had no significant effects on cell viability, skeleton and proliferation when diluted 128-fold. Results were shown as Mean ± SD; One-way ANOVA; n = 6; * indicates statistical difference ($P < 0.05$), ** means $P < 0.01$, *** means $P < 0.001$.

characterized by XRD (Fig. 2I), with BSG serving as the reference. At 7 days in PBS, a broad diffraction peak (at about 2 θ = 35°) was observed in all BSG + Fe_3O_4 groups, corresponding to the reference BSG. And BSG + 5%Fe_3O_4 group exhibited the most prominent diffraction peak at all time points compared to other scaffolds.

3.2. *In vitro effects of BSG + Fe_3O_4 magnetic scaffold extracts on cytotoxicity, proliferation, viability and cytoskeleton of MSCs*

The results of the CCK8 assay reveals that a stark decline in MSCs viability when exposed to the undiluted BSG + Fe_3O_4 magnetic scaffold extracts ($P < 0.0001$) (Fig. 3A). Consequently, we undertook serial dilutions of the BSG + Fe_3O_4 magnetic scaffold extracts, incrementally reducing their concentration by factors of 2 with cell culture medium. After 1 day incubation with extract concentrations, the CCK8 assay indicated a persistent inhibition of cell survival significantly, even at dilutions of 2-, 4-, 8-, 16-, 32- and 64-fold, with a concomitant increase in cell survival as extract concentration decreased significantly ($P < 0.0001$) (Fig. 3B–G). Notably, an obvious rise in cells survival rate was not observed until the extract was diluted 128 times ($P = 0.6602 > 0.05$) (Fig. 3H–I). To validate our findings, we replicated the CCK8 assay using higher extract dilutions. Interestingly, we found that the BSG + 5% Fe_3O_4 magnetic scaffold extracts exhibited minimal impact on cell proliferation when diluted 128-fold ($P = 0.3957 > 0.05$) (Fig. 3J–M).

Additionally, fluorescent labeling of MSCs was employed to further assess the impact of extracts on cell proliferation, cytoskeleton, and viability using a confocal microscope. Firstly, EdU value-added staining showed no significant alternation in cell proliferation when the extracts were diluted 128-fold (Fig. 3N). Secondly, the live/dead assay revealed that the viability of cells across all BSG + Fe_3O_4 extract groups (Fig. 3O). Thirdly, cytoskeletal staining demonstrated that MSCs exposed to the extracts maintained normal cell morphology, devoid of curling, shrinkage, or fragmentation (Fig. 3P). Overall, the BSG + 5%Fe_3O_4 magnetic scaffold extracts exhibited highly biocompatibility when diluted 128 times, display no discernible effects on MSCs proliferation, morphology, or viability.

3.3. *Osteogenic induction of BSG + Fe_3O_4 magnetic scaffold extracts on MSCs in vitro*

Quantification of ALP staining demonstrated that when diluted 64-, 128- and 256-fold, all BSG and BSG + Fe_3O_4 scaffold extracts significantly promoted ALP expressions in MSCs compared to the control group, which was cultured in OIM without scaffolds extracts. The most pronounced effect was observed with the 128-fold dilution of BSG + 5% Fe_3O_4 extract ($P < 0.0001$ vs control) (Fig. 4A and C). Similarly, quantification of Alizarin red S staining yielded identical results to ALP staining. Specifically, the 128-fold dilution of BSG + 5%Fe_3O_4 extract exerted the most substantial impact on late matrix mineralization ($P < 0.0001$ vs control) (Fig. 4B and D).

The expression of osteogenesis related mRNA (RUNX2, ALP, OCN) (Fig. 4E and F) and proteins (RUNX2 and OCN) (Fig. 4G and H) were assessed via RT-qPCR and Western blot, with quantification of the blot results displayed in Fig. 4I and J. Consistent with the findings elsewhere of this study, the extracts from all BSG and BSG + Fe_3O_4 scaffold formulations exhibited upregulated expression of osteogenic genes and proteins at a 128-fold dilution concentration. More specifically, the 128-fold dilution of BSG + 5%Fe_3O_4 scaffold extracts exhibited the most significant upregulation of osteogenic genes ($P < 0.0001$ vs control).

3.4. *RNA transcriptome sequencing of MSCs cultured with BSG + 5% Fe_3O_4 extract to assess expression of immune, osteogenic, and inflammatory genes in vitro*

MSCs were cultured in OIM with or without 128-fold dilution of BSG + 5%Fe_3O_4 magnetic scaffold extract for 7 days, RNA transcriptome sequencing was performed to analyze gene expression profiles compared with negative control (Fig. 5A and B). The GO enrichment bubble map revealed that BSG + 5%Fe_3O_4 magnetic scaffold extracts notably enhances the expression of genes associated with the immune response of MSCs to viruses and bacteria (Fig. 5C and D, red boxes), as well as genes related to osteogenic differentiation, extracellular matrix secretion, and bone tissue mineralization (Fig. 5C and D, blue boxes). Additionally, the scaffold extract promoted the expression of gene linked to chemokine receptor related pathways, such as CCR2, which mediate inflammation (Fig. 5C, green boxes). These sequencing results suggest that BSG + 5% Fe_3O_4 magnetic scaffold extract holds promise for exerting immunomodulatory and osteogenic effects within the local MSC population. The molecular pathways of differentially expressed genes were further investigated using KEGG enrichment. The findings revealed that BSG + 5%Fe_3O_4 magnetic scaffold extract significantly upregulated the expression of genes associated with the NOD-like receptor (NLR) and TNF signaling pathways in MSCs (Fig. 5E and F, red boxes). This confirmation underscores the potential of the magnetic scaffold to modulate bone immunity and regulate bone homeostasis.

3.5. *Polarization and inflammation-related genes expression of RAW 264.7 in vitro*

RAW 264.7 cells were cultured with 128-fold dilution of scaffold extract for 3 days, followed by flow cytometry for CD80 and CD206. The expression of the M1 phenotype marker, CD80, was notably diminished (Fig. 6A), while the expression of the M2 phenotype marker, CD206, was enhanced in the BSG and BSG + Fe_3O_4 magnetic scaffold extract groups compared to the control group (Fig. 6B). Among the scaffold extracts, the expression of CD80 in BSG group (79.73 %) was only lower than control group (82.97 %), the expression of CD206 in BSG group (52.77 %) was also only higher than control group (49.34 %). Notably, the BSG + 5%Fe_3O_4 group showed the lowest expression (70.97 %) of CD80 and the highest expression (58.65 %) of CD206. Subsequently, we assessed the expression of inflammation-related genes in macrophages using RT-qPCR. Compared to the control group, RAW 264.7 macrophages cultured with the128-fold dilution of BSG magnetic scaffold extract media demonstrated elevated expression of anti-inflammatory genes (TGF-β1: $P = 0.9928$ and IL-1Ra: $P < 0.0001$) (Fig. 6C) and lower expression of pro-inflammatory genes (IL-6: $P = 0.5749$ and IL-1β: $P < 0.0001$) (Fig. 6D). Moreover, BSG + 5%Fe_3O_4 had the significantly promotion effect on expression of TGF-β1 ($P = 0.0038$ vs control, $P = 0.0012$ vs BSG) and IL-1Ra ($P < 0.0001$ vs control, $P = 0.0133$ vs BSG) (Fig. 6C), and the most obvious inhibition effect on IL-6 ($P < 0.0001$ vs control, $P < 0.0001$ vs BSG) and IL-1β ($P < 0.0001$ vs control, $P < 0.0001$ vs BSG) (Fig. 6D). These findings suggest that the incorporation of Fe_3O_4 nanoparticles into BSG may synergically attenuate the inflammatory response among macrophages.

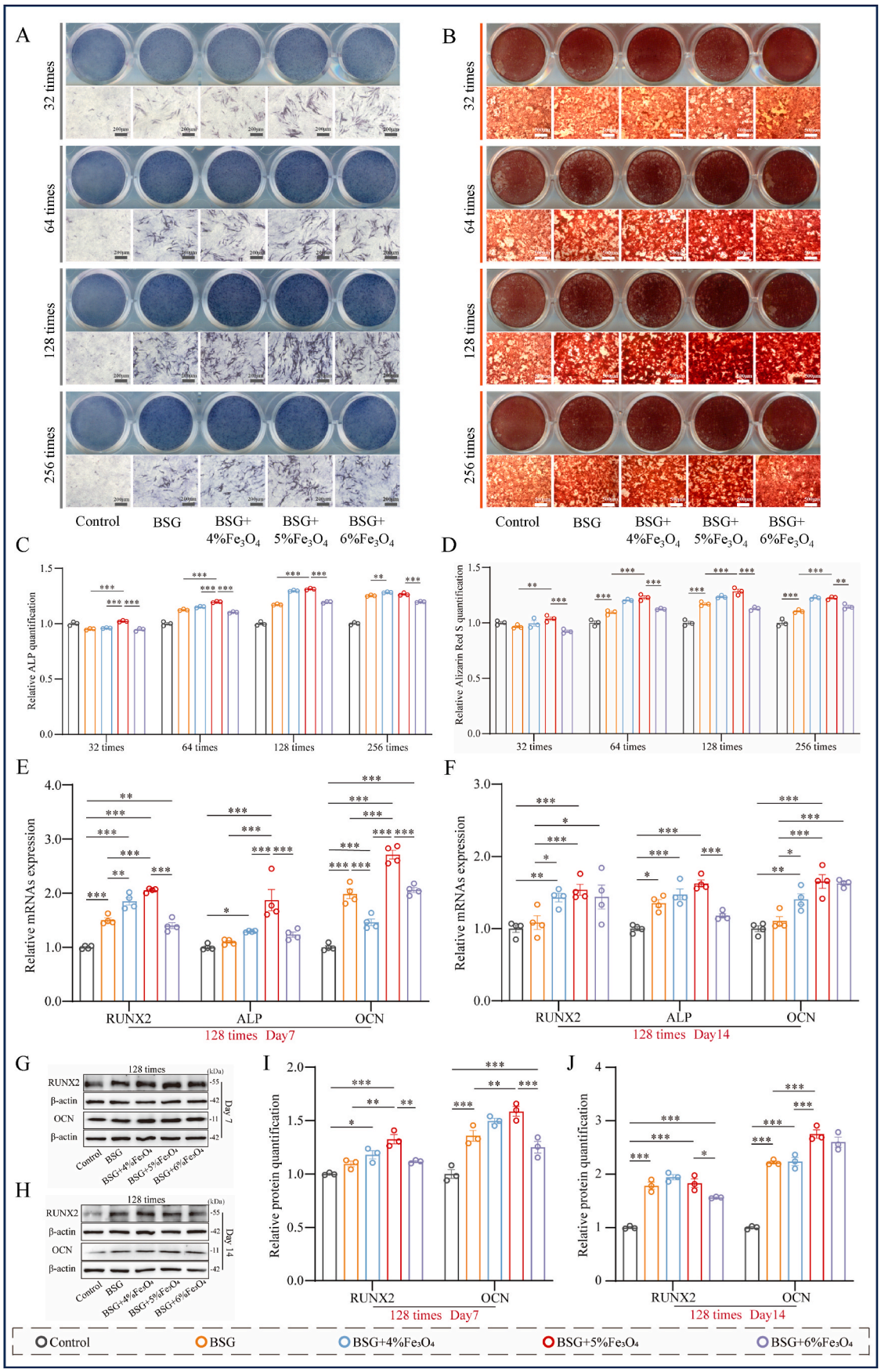

(caption on next page)

Fig. 4. Osteogenic effects of BSG extracts at 128-fold dilution on MSCs and macrophages in culture. A) ALP staining of MSCs (C3H10T1/2) cultured with scaffold extracts DMEM diluted 32-, 64-, 128-, and 256-fold in OIM for 7 days, and B) alizarin red S staining after 21 days of culture, C-D) with corresponding quantitative analysis (n = 3). Specifically, the 128-fold dilution of BSG + 5%Fe_3O_4 extract exerted the most substantial impact on ALP activity and late matrix mineralization. E-F) The expression of osteogenesis related mRNA (RUNX2, ALP, OCN) (n = 4) and G-H) proteins (RUNX2 and OCN) were assessed via RT-qPCR and Western blot, with quantification of the blot results displayed in I and J (n = 3). The results suggested that the 128-fold dilution of BSG + 5%Fe_3O_4 scaffold extracts exhibited the most significant upregulation of osteogenic genes. Results were shown as Mean ± SD; Two-way ANOVA; * indicates statistical difference ($P < 0.05$), ** means $P < 0.01$, *** means $P < 0.001$.

3.6. Evaluation of magnetic-thermal-induced thermal response of BSG + Fe_3O_4 ex vivo

Thermal images of each scaffold were captured over time-course using a far-infrared thermometer (Fig. 7A and D), and the data were analyzed using AnalyzIR. When subjected to AMF for 180 s, the temperatures of BSG + 4%Fe_3O_4, BSG + 5%Fe_3O_4, and BSG + 6%Fe_3O_4 reached 46.1 ± 0.7 °C, 54.7 ± 1.1 °C, and 65.3 ± 1.2 °C, respectively (Fig. 7B). Additionally, we observed a radial decrease in temperature of the surrounding air or rabbit tibia due to thermal diffusion. Linear regression analysis demonstrates a decrease in temperature from the center of the interface of BSG + 5%Fe_3O_4 magnetic scaffold radially outward into the air ($P = 0.0621$, r = −0.4616, 95%CI, −0.7712 to 0.02446) (Fig. 7E). In the fresh rabbit tibia, the central temperature of BSG + 5%Fe_3O_4 reached 54.7 ± 1.1 °C when exposed to AMF for 180 s. Previous studies have established that the minimal effective temperature for sterilization is approximately 45 °C [19], and that this temperature dose not damage to the host tissue. According to the linear regression of temperature attenuation from the center of BSG + 5% Fe_3O_4 interface, the effective sterilization temperature of 45 °C was achieved at an average radial distance of 0.1155 mm ($P < 0.0001$, r = −0.9654, 95%CI, −0.9861 to −0.9150) (Fig. 7F and G).

3.7. Antibacterial activity of BSG + 5%Fe_3O_4 in vitro

Based on the assessment of cytotoxicity, inductive effects on MSCs and macrophages, and thermal responsiveness of all BSG + Fe_3O_4 scaffolds, BSG + 5%Fe_3O_4 magnetic scaffold was chosen for further antibacterial experiments *in vitro*. PMMA bone cement exhibited no inhibitory effect on *S. aureus* in TSA plates. However, BSG, BSG + 5% Fe_3O_4 and BSG + 5%Fe_3O_4 + AMF (180 s) demonstrated some antibacterial effects (Fig. 7H). The diameters of the zones of inhibition were measured for each group (n = 5), revealing that BSG + 5%Fe_3O_4 exhibited the most pronounced antibacterial effect after 180 s AMF treatment ($P < 0.0001$) (Fig. 7I). This finding aligns with the thermal bactericidal mechanism associated with iron oxide nanoparticles.

3.8. Ex vivo representative gross images and CT of BSG + 5%Fe_3O_4 scaffold at day 42

The design of 1-stage revision bone infection model is illustrated in Fig. 8A. Rabbits were euthanized on days 7 and 42 after treatment, and gross images of the superior tibial metaphysis were collected. On day 7, all specimens exhibited well-maintained scaffold positioning without displacement or prolapse, while soft tissue swelling and pus moss formation were observed in all groups (Fig. 8B). By day 42, pus (yellow arrow) and soft tissue infection (orange arrow) were present at the screw tract in the untreated and BSG + 5%Fe_3O_4 groups, and with a noticeable reduction in the diameter of the screw tract compared to 7 days. In contrast, pus was absent in the BSG + 5%Fe_3O_4 + AMF group, and the screw tract had nearly disappeared (red arrow) by day 42 (Fig. 8C).

The CT image (Fig. 8D) of the untreated group displayed evident periosteal response (green arrow) and osteolytic destruction or formation of dead bone (orange arrow) in the medullary cavity on days 28 and 42. Periosteal response was also observed in cortical bone on days 7, 14 and 28 in the BSG + 5%Fe_3O_4 group (green arrows), while a noticeable periosteal reaction was absent in the BSG + 5%Fe_3O_4 + AMF group. By day 42, the BSG + 5%Fe_3O_4 and BSG + 5%Fe_3O_4 + AMF groups exhibited cortical bone healing (red arrows) at the implant site. Taken together, these CT results suggest that BSG + 5%Fe_3O_4 scaffold with AMF exhibited the excellent antibacterial activity of this infection model with 42 days, which significantly inhibited the corresponding inflammation response and subsequent periosteal response that caused by *S. aureus* compared to BSG + 5%Fe_3O_4 alone.

3.9. Histology of infected tibiae to assess antibacterial and osteogenic effects of BSG + 5%Fe_3O_4 + AMF in vivo

On day 7 post-primary infection surgery, histological evidence of bone infection could be observed in both the untreated and the BSG + 5%Fe_3O_4 groups, as illustrated by H&E and Gram staining (Fig. 9A). Significant hemorrhage was observed around the screw tract in the untreated group, with evidence of *S. aureus* colonized within OLCN and biofilm formation still visible around the primary infection site (red arrows) (Fig. 9A). Furthermore, SACs were observed around the scaffolds in the BSG + 5%Fe_3O_4 group (Fig. 9B). The black arrows indicate possible undegraded iron in the scaffolds. These findings are indicative of the persistence of SACs and bacterial colonies within OLCN in the untreated control rabbits and those implanted with the BSG + 5%Fe_3O_4 scaffold after one day of infected screw removal and debridement procedures. This underscores the insufficiency of debridement alone in eliminating those bacteria within biofilms.

On day 28, the infection sites had progressed to diffuse inflammatory lesions in both the untreated and BSG + 5%Fe_3O_4 groups, with the infection spreading throughout the medullary cavity (green arrows) and extensive cortical osteolysis around the screw tract (blue arrow). Notably, substantial SACs formation was observed in the pulp cavity of the untreated group (red arrows). In the BSG + 5%Fe_3O_4 group, *S. aureus* was detected around and within the scaffold (red arrow) (Fig. 9C and D). In contrast, the scaffold and pulp cavity of the BSG + 5%Fe_3O_4 + AMF group exhibited minimal bacterial presence and clear signs of fibrous membrane wrapping around the scaffold, indicative of early bone formation (Fig. 9E).

At 42 days post-treatment, H&E and Gram staining revealed partial degradation of the BSG + 5%Fe_3O_4 scaffold and a reduction in the diffuse medullary lesions observed on day 28 (green arrows). However, some bacteria persisted within the scaffolds (red arrows) (Fig. 9F). Remarkably, the BSG + 5%Fe_3O_4 + AMF group exhibited significant new bone deposition (yellow arrows) and pronounced scaffold degradation (Fig. 9G). Overall, the results of histological staining on day 28 and day 42 demonstrated that the implantation of BSG + 5%Fe_3O_4 alone can inhibit bacterial growth to a certain extent but cannot effectively eliminate bacteria completely. However, for those rabbits treated with BSG + 5%Fe_3O_4 scaffold with an AMF, there was a visible reduction in *S. aureus* in the medullary cavity, along with notable enhancements in new bone formation and scaffold degradation.

4. Discussion

Since bone infections can lead to severe progressive osteolysis, the treatment for osteomyelitic defects must prioritize infection control to create aseptic conditions that promote bone healing. *S. aureus* bone infection is particularly challenging due to the formation of biofilms, including colonization of the OLCN and formation of SACs, which complicates control and control on efforts.

Our previous studies have shown that PMMA + Fe_3O_4 combined with

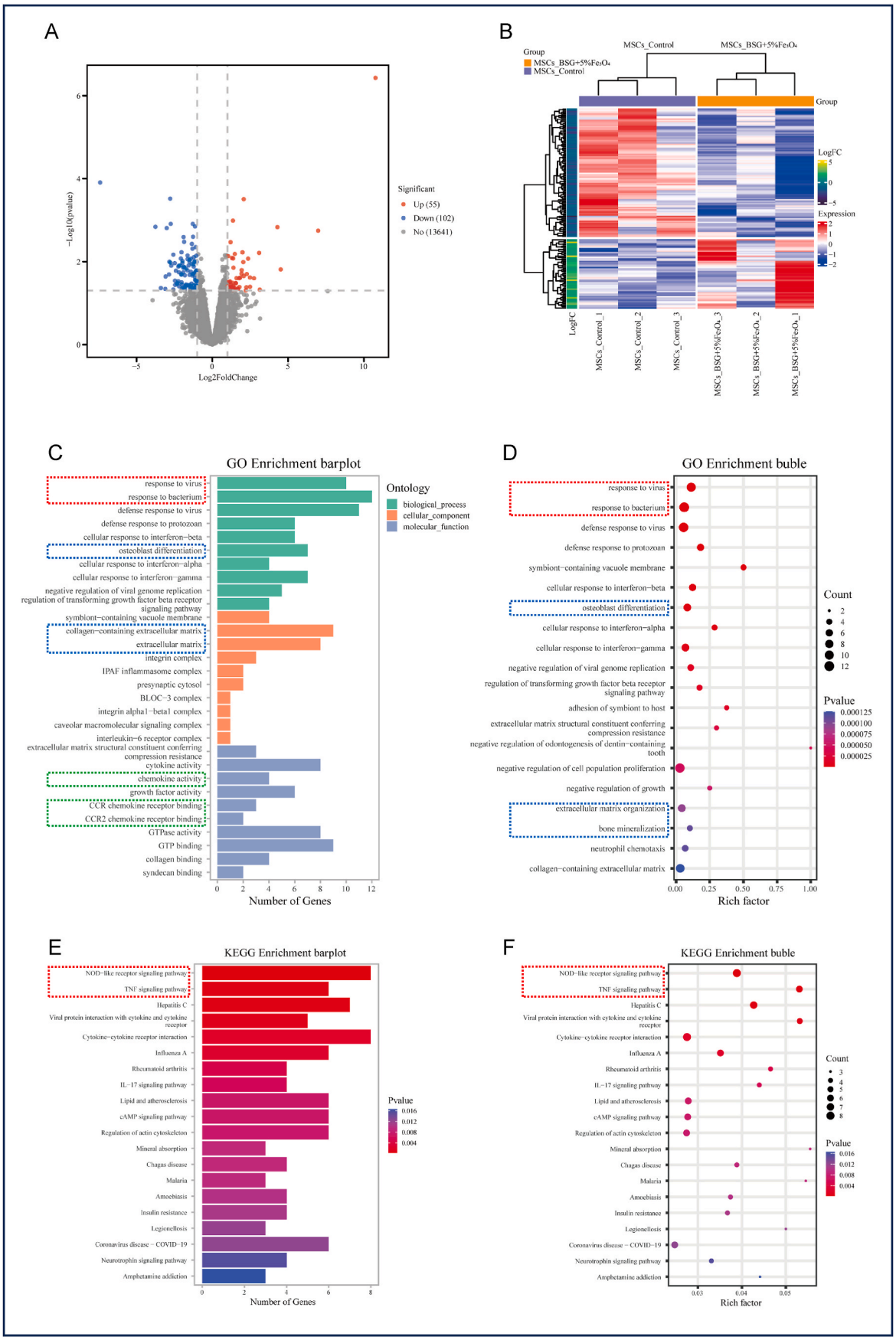

(caption on next page)

Fig. 5. BSG + 5%Fe_3O_4 enhances immune response to bacteria, osteogenic differentiation, and chemokine receptor gene expression in MSCs. A-B) MSCs (C3H10T1/2) were cultured in 128-fold dilution of BSG + 5%Fe_3O_4 extract for 7 days, and RNA transcriptome sequencing was performed on three separate samples, along with three unexposed MSCs as negative controls. Genes with significant changes in transcript numbers and high p-values were selected using a thresholding method. C-D) GO enrichment bubble map revealed enrichment of genes associated with the immune response of MSCs to viruses and bacteria (red boxes), osteoblast differentiation, extracellular matrix secretion, bone tissue mineralization (blue boxes), as well as chemokine receptor related pathways (such as CCR2) involved in mediating inflammation response (green boxes). E-F) The molecular pathways of differentially expressed genes were further investigated using KEGG enrichment, these findings revealed that BSG + 5%Fe_3O_4 **magnetic scaffold** extract significantly upregulated the expression of genes associated with the NOD-like receptor (NLR) and TNF signaling pathways in MSCs (red boxes). This confirmation underscores the potential of the magnetic scaffold to modulate bone immunity and regulate bone homeostasis.

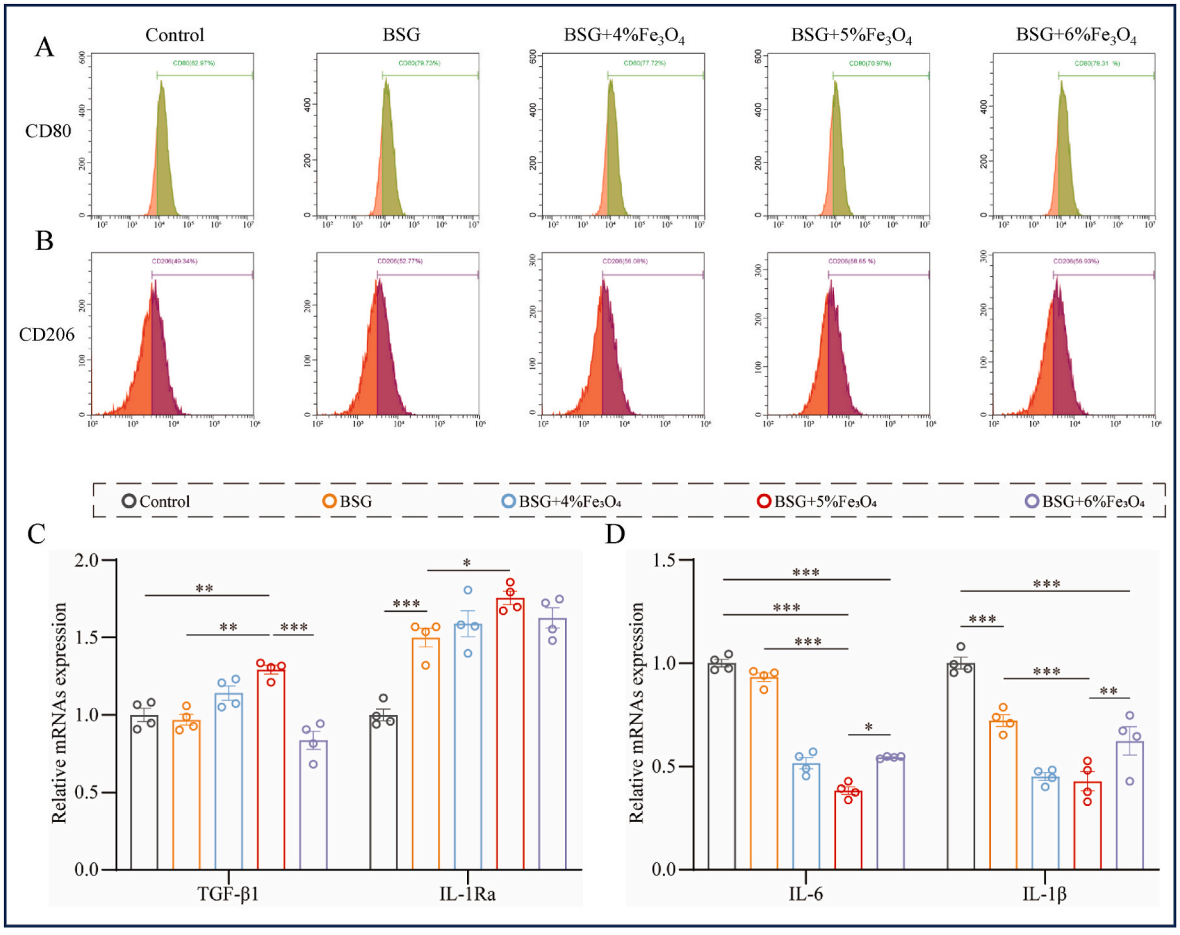

Fig. 6. BSG scaffolds regulate inflammation in macrophages *in vitro*. A-B) **RAW 264.7 cells were cultured with 128-fold dilution of scaffold extract for 3 days,** followed by flow cytometry for CD80 and CD206, **the BSG + 5%Fe_3O_4 group showed the lowest expression (70.97 %) of CD80 and the highest expression (58.65 %) of CD206.** C-D) The expression of anti-inflammatory (TGF-β1 and IL-1Ra) and pro-inflammatory (IL-6 and IL-1β) gene in macrophages were **assessed by** RT-qPCR. **Compared to the control group, RAW 264.7 macrophages cultured with the128-fold dilution of BSG + 5%Fe_3O_4 had the significantly promotion effect on expression of TGF-β1and IL-1Ra, and the most obvious inhibition effect on IL-6 and IL-1β.** Results were shown as Mean ± SD; Two-way ANOVA; * indicates statistical difference ($P < 0.05$), ** means $P < 0.01$, *** means $P < 0.001$.

AMF therapy can mitigate osteolysis caused by *S. aureus* bone infection [19]. However, the traditional antibiotic bone cement cannot be degraded, necessitating the development of materials with greater osteogenic potential. To address this, we constructed a composite material capable of magnetothermal therapy using Fe_3O_4 and BSG, and evaluated its antibacterial properties and osteogenic capacity both *in vitro* and in a one-stage revision model of rabbit bone infection.

Magnetic particle hyperthermia (MPH) utilizes the interaction between magnetic fields and magnetic nanoparticles (MNPs) to generate heat to achieve anti-cancer and antibacterial effects [31]. Previous studies have demonstrated that temperatures of 45 °C–60 °C are capable of killing planktonic bacteria [32,33] and inhibiting the formation of biofilms [34–36]. In the context of soft tissue therapy, the safe hyperthermia range typically falls between 42 °C and 48 °C [37–40]. Our prior research has shown that exposure of PMMA + Fe_3O_4 to an AMF for 180 s *in vitro* resulted in a temperature of 56 ± 0.7 °C *in vivo*. Moreover, *in vivo* experiments have shown its efficacy in killing *S. aureus*, with histopathological analyses revealing no damage to bone tissue [2]. These findings underscore the potential of PMMA + Fe_3O_4 combined with AMF therapy as a promising approach for combating *S. aureus* bone infection. Recently, while there are reports utilizing AMF in conjunction with magnetic nanoparticles for antibacterial therapy too [41–45], limited research has delved into the mechanisms underlying bacterial clearance with AMF. For instance, Kim et al. demonstrated the efficacy of MNP/AMF hyperthermia in targeting and inhibiting the growth of bacterial pathogen using both *in vitro* and *in vivo* models of *S. aureus* biofilm infection. However, they did not delve into the mechanisms driving bacterial clearance with AMF [46]. Previous studies have

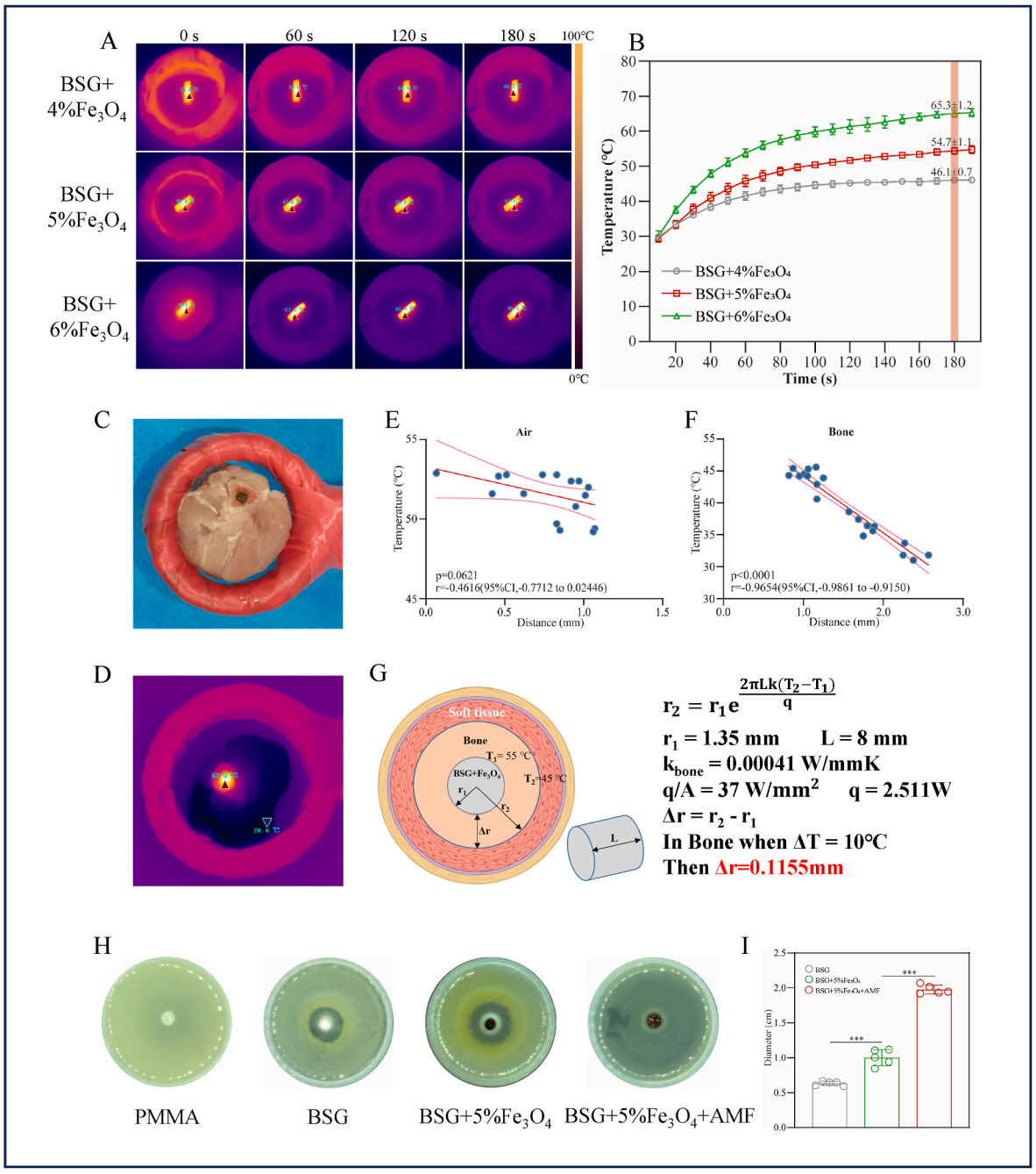

Fig. 7. Magnetic-thermal-induced thermal efficiency and antibacterial properties of BSG + Fe_3O_4 *in vitro*. A, D) Thermal images of each scaffold were captured over time-course using a far-infrared thermometer. B) When subjected to AMF for 180 s, the temperatures of BSG + 4%Fe_3O_4, BSG + 5%Fe_3O_4, and BSG + 6%Fe_3O_4 reached 46.1 ± 0.7 °C, 54.7 ± 1.1 °C, and 65.3 ± 1.2 °C, respectively. C) White light image of the tissue sample under AMF. E) Linear regression analysis of temperature change from the center of the interface of BSG + 5%Fe_3O_4 magnetic scaffold radially outward into the air when exposed to AMF for 180 s. F) In the fresh rabbit tibia, linear regression is drawn according to the attenuation of BSG + 5%Fe_3O_4 interface center temperature with distance. when exposed to AMF for 180 s. G) According to the linear regression of temperature attenuation from the center of BSG + 5%Fe_3O_4 interface, the effective sterilization temperature of 45 °**C** was achieved at an average radial distance of 0.1155 mm. H–I) Antibacterial properties of each scaffold *in vitro* and statistical analysis of diameter of bacteriostatic zone. inhibition zone of BSG + 5%Fe_3O_4 + AMF exhibited the largest zone of inhibition against *S. aureus* on **TSA plate. Results are shown as Mean± SD; One-way ANOVA; *indicates statistical difference (*P*<0.05), *** means *P*<0.001.**

revealed that MNP/AMF-induced heat shock in *S. aureus* biofilm cultures can significantly enhance antibiotic uptake by the bacterial biofilm phase. This response is not dependent on antibiotic penetration through the biofilm matrix [47]. Additionally, gene microarray data obtained from the culture of *S. aureus* biofilm suggest that mild MNP/AMF can shift the expression of genes involved in cellular respiration from anaerobic fermentation to an aerobic glycolytic/tricarboxylic acid cycle (TCA) pathway. This implicates that the beneficial effect of mild MNP/AMF hyperthermia on increasing susceptibility of biofilm bacteria to antibiotic treatment is associated with increased metabolic activity [48]. The biological mechanism underlying the efficacy of the magnetic bioactive scaffold developed in this study for bacterial clearance in an AMF remains unclear. In forthcoming research endeavors, we aim to address this scientific gap by employing *in vitro* SACs biofilm models in conjunction with *in vivo* evidence of antibacterial efficacy.

In our endeavor to introduce BSG as an alternative to PMMA bone

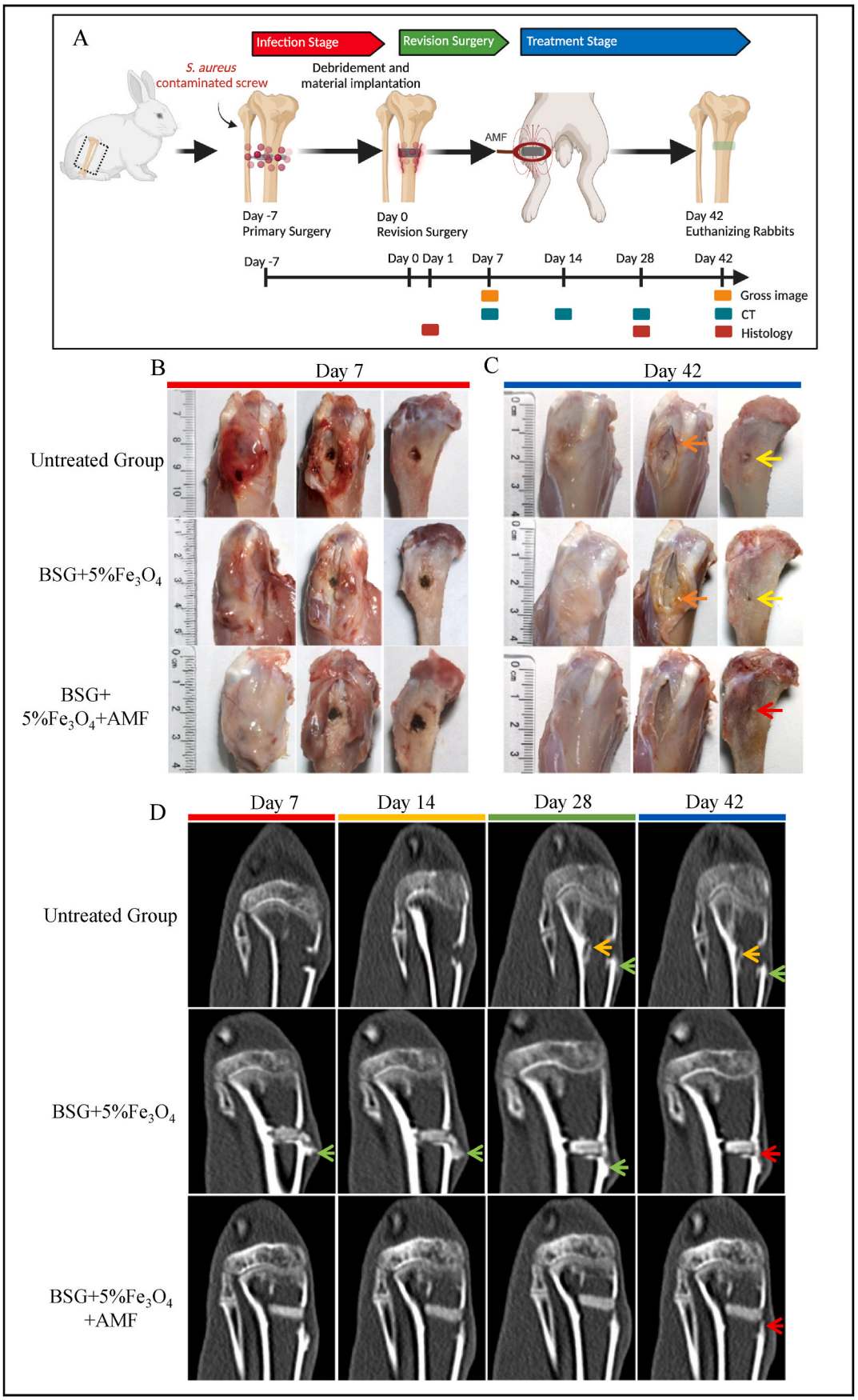

(caption on next page)

Fig. 8. Representative gross images and CT images of infected tibiae with untreated group, BSG + 5%Fe_3O_4 or BSG + 5%Fe_3O_4 + AMF as far as 42 days. A) The design of 1-stage revision bone infection model. B) Gross images of the superior tibial metaphysis on days 7. All specimens exhibited well-maintained scaffold positioning without displacement or prolapse, while soft tissue swelling and pus moss formation were observed in all groups. C) Gross images of the superior tibial metaphysis on days 42. By day 42, pus (yellow arrow) and soft tissue infection (orange arrow) were present at the screw tract in the untreated and BSG + 5%Fe_3O_4 groups, and with a noticeable reduction in the diameter of the screw tract compared to 7 days. In contrast, pus was absent in the BSG + 5%Fe_3O_4 + AMF group, and the screw tract had nearly disappeared (red arrow) by day 42. D) CT images of rabbit tibiae on days 7, 14, 28, and 42 post revision. On days 28 and 42, the untreated group displayed evident periosteal response (green arrow) and osteolytic destruction or formation of dead bone (orange arrow) in the medullary cavity. Periosteal response was also observed in cortical bone on days 7, 14 and 28 in the BSG + 5%Fe_3O_4 group (green arrows), while a noticeable periosteal reaction was absent in the BSG + 5%Fe_3O_4 + AMF group. On day 42, the BSG + 5%Fe_3O_4 and BSG + 5%Fe_3O_4 + AMF groups exhibited cortical bone healing (red arrows) at the implant site.

cement, we were imperative to ascertain whether the bactericidal effects of Fe_3O_4-mediated thermomagnetic therapy exhibited comparable efficacy, particularly in bone and soft tissue. To address this, we constructed an *ex vivo* model utilizing fresh tibia of rabbit to explore the effective bactericidal distance and thermal diffusion profile of BSG + 5%Fe_3O_4. In this study, the scaffold was positioned at the center of the bone marrow, and the tissue samples were subjected to heating for 180 s under an AMF, while monitoring temperature changes over time and across the specimen area. Our findings revealed that when the temperature of BSG + 5%Fe_3O_4 reached approximately 55 °C, a zone of effective bactericidal temperature (>45 °C) extended by 0.1155 mm from the scaffold within the bone tissue. Importantly, none of the soft tissue experienced temperatures exceeding the safe hyperthermia limit of 48 °C.

While the RNA transcriptome sequencing of MSCs and RT-qPCR of RAW 264.7 cells have indicated immunomodulatory and osteoinductive properties of BSG + 5%Fe_3O_4, further investigation is required to understand the etiology of such signaling and *in vivo* manifestations. An important aspect to consider is whether the M2 polarization of macrophages contributes positively to the unique clinical situation of osteomyelitis defects. Although the activation of cellular immunity (M1) may seem imperative for controlling infection, we suggest that M2 polarization holds greater overall therapeutic potential, particularly as osteomyelitis often presents with large defects where stability loss and non-union are major concerns. Furthermore, a common challenge in *S. aureus* osteomyelitis is the failure of cellular immunity in controlling OLCN colonies. Despite this, the unique combination of anti-inflammatory immunomodulation with the novel antibacterial mechanism of Fe_3O_4 nanoparticles represents a promising balance for addressing the challenges of infectious defects.

BSG is a well-studied material in the field of bone tissue engineering due to its ability to induce osteogenesis and modulate macrophage polarization through ion release mechanisms [49]. The incorporation of boron and silicon into bioactive glass facilitates rapid exchange ions with bodily fluids and subsequent precipitate of matrix ions, thereby accelerating the formation of ionic and alkaline microenvironments [50]. The alkaline microenvironment not only fosters osteogenesis by modulating immune regulation [51], but also impedes bacterial energy metabolism and kills bacteria ultimately [52]. Some studies have demonstrated that bioactive glass, such as S53P4, are safe and effective in treating of osteomyelitis and can control infections caused by multidrug-resistant *S. aureus* strains [53]. Upon implantation into patient's infectious bone defects, the bioactive glass product has demonstrated a high infection cure rate ranging from 70.3 % to 90 %, underscoring the reliable therapeutic effects of BSG in bone infection treatment [54–57]. Regarding the potential antibacterial mechanisms of BSG, Marques and colleagues has reported that the initial suppression of bacterial biofilm formation by BSG may stem from their degradation products and the creation of a local alkaline microenvironment [58]. Furthermore, our previous research have demonstrated that Fe_3O_4--loaded BSG scaffolds exhibit greater bone regeneration capacity, making them suitable for repairing bone defects resulting from conditions as tumor resection [23]. Drawing from the evidence outline above, we consider the development of a BSG + Fe_3O_4 scaffold as an alternative approach for the treatment of *S. aureus* bone infection with biofilm formation.

In the context of this study, iron oxide nanoparticles (IONPs) exhibit multifaceted mechanisms of bactericidal activity [59,60]. Firstly, when subjected to the appropriate AMF regimen, IONPs can convert magnetic energy into heat energy to sterilize the implant site without causing tissue damage [61]. Secondly, IONPs possess intrinsically bactericidal properties. Fe^{3+} ions not only disrupt bacterial cell wall via surface charge interactions but also increase ROS level within bacteria [62,63]. Our results indicate that BSG + 5%Fe_3O_4, even without an AMF, exhibited certain bactericidal and osteogenic effects *in vivo*. However, some bacteria persisted within the OLCN and SACs, resulting in infectious bone defects. With daily AMF therapy, bacteria were controlled completely at the interface and medullary cavity of material, accompanied by observed new bone formation within and surrounding the implant, as well as partial degradation of the material. While this may be attributed to the presence of an osteoconductive surface for periosteal differentiation and deposition, it is also plausible that the chemical properties of the scaffold and the antibacterial effect after AMF treatment contributed to osteogenesis. Indeed, our *in vitro* examination of MSCs and macrophage differentiation suggests such effects via mechanisms yet to be fully elucidated.

Some scholars indicated that IONPs have superior biocompatibility and stability, with minimal intrinsic toxicity [64]. However, concerns have been raised regarding the potential hepatotoxicity associated with the engulfment of IONPs [65]. In this study, the cytotoxic assessment using the CCK8 assay showed that the BSG + 5%Fe_3O_4 extract, even at a 128-fold dilution, had no significant effect on cell viability. Moreover, the live/dead staining showed that there was no significant change in cell morphology or viability compared to the control group. Cytoskeletal staining also showed that MSCs exhibited normal cell morphology without curling, shrinking, or fragmentation. And after 128-fold dilution, BSG + 5%Fe_3O_4 extract had significant effects on osteogenic differentiation, macrophage M2 polarization, and immune regulation. Even our *in vivo* findings demonstrated the obvious osteoinductive properties of BSG + Fe_3O_4 scaffolds post implantation, without any complications such as local inflammation or visceral fibrosis. However, we acknowledge the inherent limitations of the current evidence. We think that the observed toxicity with high-concentration extracts in *in vitro* models arises from the rapid release of ions in a confined microenvironment. Contrastingly, during *in vivo* experiments, this toxicity is anticipated to diminish owing to the metabolic processes of blood and tissue fluid, thereby lowering the likelihood of adverse reactions. Therefore, it is essential to conduct further investigations to validate whether the extracts of the scaffold, metabolized by tissue fluid and disseminated to other organs, might indeed provoke toxic effects. To bridge the gap between the reliability of *in vitro* toxicity experimental detection models and *in vivo* toxicity detection, we plan to administer intravenous treatments to healthy animals using extracts with various dilutions. This approach will be complemented by a comprehensive array of coupled parameters, including clinical serology, imaging, and histology, enabling us to systematically evaluate the impact of different dilution ratios of extracts on liver and kidney toxicity, as well as on stem cell osteogenic properties, growth plates, and osteoclasts in healthy animals. By employing a comprehensive approach that integrates both *in vitro* and *in vivo* assessments, we aim to gain a more thorough understanding of the effects of these extracts on various physiological systems, ultimately enhancing the reliability and relevance of our findings. Furthermore, Histological evidence did not observe any

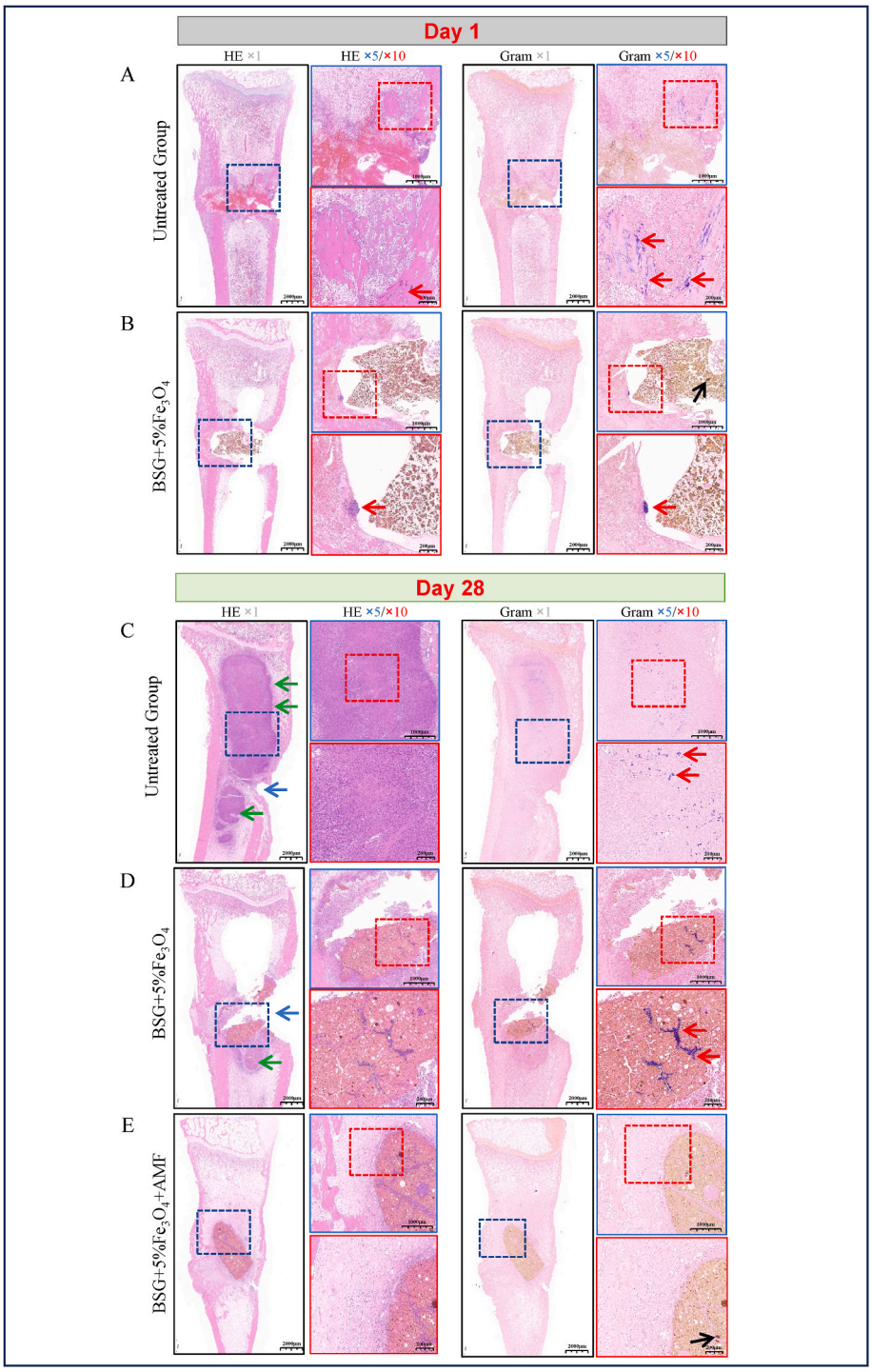

Fig. 9. Histological evidence of the antibacterial effects of BSG + 5%Fe_3O_4 *in vivo*. A) H&E and Gram staining after infection surgery for 7 days, histological evidence of bone infection could be observed in both the untreated and the BSG + 5%Fe_3O_4 groups (red arrows). SACs were observed around the scaffolds of BSG + 5%Fe_3O_4 group, and undegraded iron was also seen in BSG + 5%Fe_3O_4 group (black arrows). C-E) H&E and Gram staining at 28 days after infection. On day 28, the infection sites had progressed to diffuse inflammatory lesions in both the untreated and BSG + 5%Fe_3O_4 groups (green arrow), and osteolysis occurred in the two groups (blue arrow). Substantial SACs formation was observed in the pulp cavity of the untreated group (red arrows). In the BSG + 5%Fe_3O_4 group, *S. aureus* was detected around and within the scaffold (red arrow). In contrast, the scaffold and pulp cavity of the BSG + 5%Fe_3O_4 + AMF group exhibited significantly reduced signs of bone infection and early bone formation. F-G) At 42 days post-treatment, H&E and Gram staining revealed partial degradation of the BSG + 5%Fe_3O_4 scaffold and a reduction in the diffuse medullary lesions observed on day 28 (green arrows). However, some bacteria persisted within the scaffolds (red arrows). Remarkably, the BSG + 5%Fe_3O_4 + AMF group exhibited significant new bone deposition (yellow arrows) and pronounced scaffold degradation.

transfer of Fe ion. With further research on BSG + Fe_3O_4 scaffold, if issues regarding its degradation rate and degradation products can be resolved, it may potentially be used in the future for the treatment of bone defects or implant-related *S. aureus* osteomyelitis. This could reduce patient treatment costs and promote early recovery while controlling the infection.

Indeed, we acknowledge several limitations in our study that warrant consideration. Firstly, the conclusions drawn from our *in vivo* study

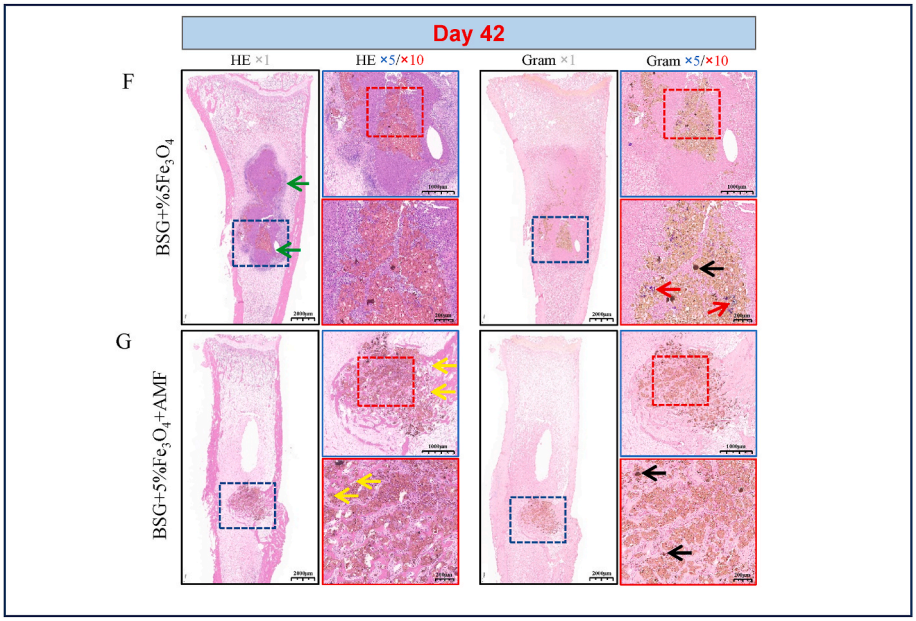

Fig. 9. (*continued*).

are based on the evidence available at present. To enhance the evaluation of the scaffold's therapeutic efficacy against bone infection, we plan to systematically conduct isolation, culture, and quantitative analysis of bacteria in local tissues. Secondly, the mechanism underlying the degradation of BSG + Fe_3O_4 products remains unclear, prompting further exploration through sequencing techniques. Concurrently, we aim to investigate the *in vivo* degradation rate of these scaffolds in future studies. Thirdly, there is a dearth of comprehensive biosafety research concerning BSG + Fe_3O_4 scaffolds. *In vitro* studies have hinted at cytotoxicity at high ion concentrations, emphasizing the need for further examination of *in vivo* biosafety and ion diffusion profiles. Lastly, we recognize limitations in histological staining due to the unavailability of suitable antibodies and reagents for rabbits. Our future research involves exploring alternative animal models to observe dynamic changes in osteoblasts, osteoclasts, and macrophages around the infection site. By addressing these limitations, we aim to not only deep the understanding of the scaffold's *in vivo* biosafety and compatibility but also contribute to a more comprehensive evaluation of its therapeutic potential.

5. Conclusion

Collectively, the BSG + 5%Fe_3O_4 magnetic scaffold investigated in this study exhibited the favorable properties in enhancing osteogenic and inflammatory pathways in MSCs, as well as promoting the polarization of macrophages toward M2 *in vitro*. To further evaluate its *in vivo* physical and chemical properties of this scaffold, we utilized a well-established implant-related *S. aureus* bone infection rabbit model. After 42 days of daily treatment with an AMF, we found that BSG + 5% Fe_3O_4 displayed superior antibacterial effects at the implant site, effectively controlling SACs and *S. aureus* within OLCN as evidenced by histological analysis. Moreover, BSG + 5%Fe_3O_4 + AMF promoted desirable new bone formation around the original infection site, effectively addressing the unique challenge of infectious bone defects. Importantly, the degradation rate of this bioactive scaffold matched the rate of bone formation effectively. In future research, we will a comprehensive study. Quantitative culturing of bacteria, along with testing common clinical parameters and employing additional histological staining approaches will be provided, we believe those results will provide a thorough understanding of the scaffold's biological performance. These investigations are indeed crucial for advancing our understanding of the scaffold's safety, degradation behavior, and underlying biomechanisms.

Considering the outstanding biomechanical properties, degradability, bactericidal activity, osteoinductive and immunomodulatory properties, and the low toxicity of this scaffold, it is suggested that BSG + 5% Fe_3O_4 magnetic scaffolds could serve as a promising alternative for the treatment of implant-related *S. aureus* osteomyelitis , with significant advantages such as reducing infection recurrence rates, improving patient outcomes, and lowering treatment costs.

Ethics approval and consent to participate

This study and included experimental procedures were approved by the Ethics Committee of the Second Affiliated Hospital of Chongqing Medical University. All animal housing and experiments were conducted in strict accordance with the institutional guidelines for care and use of laboratory animals.

CRediT authorship contribution statement

Ying Jin: Writing – review & editing, Writing – original draft, Validation, Software, Methodology, Investigation, Formal analysis, Data curation, Conceptualization. **Hang Liu:** Writing – review & editing, Writing – original draft, Validation, Software, Methodology, Investigation, Formal analysis, Data curation, Conceptualization. **Lei Chu:** Resources, Project administration, Methodology, Funding acquisition, Formal analysis, Data curation, Conceptualization. **Jin Yang:** Methodology, Investigation, Formal analysis. **Xiuyang Li:** Resources, Investigation. **Hang Zhou:** Methodology, Data curation, Conceptualization. **Haitao Jiang:** Software, Methodology, Investigation. **Lei Shi:** Visualization, Formal analysis, Conceptualization. **Jason Weeks:** Writing – review & editing, Methodology, Conceptualization. **Joshua Rainbolt:** Software, Conceptualization. **Changjiang Yang:** Validation, Software, Methodology. **Thomas Xue:** Visualization, Data curation, Conceptualization. **Haobo Pan:** Supervision, Resources, Formal analysis, Conceptualization. **Zhongliang Deng:** Writing – review & editing, Writing – original draft, Supervision, Methodology, Investigation, Funding acquisition. **Chao Xie:** Writing – review & editing, Supervision, Data curation, Conceptualization. **Xu Cui:** Writing – review & editing,

Writing – original draft, Supervision, Methodology, Investigation, Funding acquisition. **Youliang Ren:** Writing – review & editing, Writing – original draft, Supervision, Methodology, Investigation, Funding acquisition.

Declaration of competing interest

Haobo Pan is an editorial board member for Biomedical Technology and was not involved in the editorial review or the decision to publish this article. All authors declare that they have no known competing financial interests or personal relationships that could have appeared to influence the work reported in this paper.

Acknowledgements

The authors acknowledge the support from National Key R&D Program of China (2023YFC2416900and 2021YFC2400500), The International Postdoctoral Exchange Fellowship Program of Chongqing (2021JLPY004), The Fellowship of China Postdoctoral Science Foundation (2021M693758), National Natural Science Foundation of China (U22A20357, 52072398and 32161160327), Natural Science Foundation Postdoctoral Science Foundation Project of Chongqing (cstc2021jcyj-bsh0019), Natural Science Foundation of Chongqing (cstc2021jcyj-msxmX0134), Shenzhen Science and Technology Program (JCYJ20230807140714030). Thanks to the Chongqing Key Laboratory of Ultrasound Molecular Imaging, The Key Laboratory of Biochemistry and Molecular Pharmacology of Chongqing, Key Laboratory of Laboratory Medical Diagnostics Ministry of Education. In addition, We would like to thank the Imaging Department of the Second Affiliated Hospital of Chongqing Medical University for the help of CT scanning , We would like to thank Professor Xu Cui ‘s research group (Shenzhen Institute of Advanced Technology, Chinese Academy of Science) for assistance with the experimental technology.

References

[1] E.M. Schwarz, J. Parvizi, T. Gehrke, et al., International consensus meeting on musculoskeletal infection: research priorities from the general assembly questions, J. Orthop. Res. : Off. Publ. Orthop. Res. Soc. 37 (5) (2018), https://doi.org/10.1002/jor.24293, 2019.

[2] Y. Ren, L. Liu, D. Sun, et al., Epidemiological updates of post-traumatic related limb osteomyelitis in China: a 10 years multicentre cohort study, Int. J. Surg. 109 (9) (2023) 2721–2731, https://doi.org/10.1097/JS9.0000000000000502.

[3] P. Kong, Y. Ren, J. Yang, et al., Relapsed boyhood tibia polymicrobial osteomyelitis linked to dermatophytosis: a case report, BMC Surg. 22 (1) (2022) 156, https://doi.org/10.1186/s12893-022-01600-4.

[4] S.D. Zoller, V. Hegde, Z.D.C. Burke, et al., Evading the host response: Staphylococcus "hiding" in cortical bone canalicular system causes increased bacterial burden, Bone Res. 8 (1) (2020) 43, https://doi.org/10.1038/s41413-020-00118-w.

[5] Y. Ren, J. Weeks, T. Xue, et al., Evidence of bisphosphonate-conjugated sitafloxacin eradication of established methicillin-resistant S. aureus infection with osseointegration in murine models of implant-associated osteomyelitis, Bone Res. 11 (1) (2023) 51, https://doi.org/10.1038/s41413-023-00287-4.

[6] E.A. Masters, R.P. Trombetta, K.L. de Mesy Bentley, et al., Evolving concepts in bone infection: redefining "biofilm", "acute vs. chronic osteomyelitis", "the immune proteome" and "local antibiotic therapy", Bone Res. 7 (2019) 20, https://doi.org/10.1038/s41413-019-0061-z.

[7] E.A. Masters, G. Muthukrishnan, L. Ho, et al., Staphylococcus aureus cell wall biosynthesis modulates bone invasion and osteomyelitis pathogenesis, Front. Microbiol. 12 (2021) 723498, https://doi.org/10.3389/fmicb.2021.723498.

[8] K.L. de Mesy Bentley, R. Trombetta, K. Nishitani, et al., Evidence of Staphylococcus aureus deformation, proliferation, and migration in canaliculi of live cortical bone in murine models of osteomyelitis, J. Bone Miner. Res. : Off. J. Am. Soc. Bone Miner. Res. 32 (5) (2017) 985–990, https://doi.org/10.1002/jbmr.3055.

[9] K.D. Alder, I. Lee, A.M. Munger, et al., Intracellular Staphylococcus aureus in bone and joint infections: a mechanism of disease recurrence, inflammation, and bone and cartilage destruction, Bone 141 (2020) 115568, https://doi.org/10.1016/j.bone.2020.115568.

[10] Y. Ren, T. Xue, J. Rainbolt, et al., Efficacy of bisphosphonate-conjugated sitafloxacin in a murine model of S. aureus osteomyelitis: evidence of "target & release" kinetics and killing of bacteria within canaliculi, Front. Cell. Infect. Microbiol. 12 (2022) 910970, https://doi.org/10.3389/fcimb.2022.910970.

[11] W. Jiranek, Antibiotic-loaded cement in total hip replacement: current indications, efficacy, and complications, Orthopedics 28 (8 Suppl) (2005) s873–s877.

[12] E.M. Schwarz, A.C. Mclaren, T.P. Sculco, et al., Adjuvant antibiotic-loaded bone cement: concerns with current use and research to make it work, J. Orthop. Res. : Off. Publ. Orthop. Res. Soc. 39 (2) (2021) 227–239, https://doi.org/10.1002/jor.24616.

[13] S. Ghosh, M. Sinha, R. Samanta, et al., A potent antibiotic-loaded bone-cement implant against staphylococcal bone infections, Nat. Biomed. Eng. 6 (10) (2022) 1180–1195, https://doi.org/10.1038/s41551-022-00950-x.

[14] D. Bobo, K.J. Robinson, J. Islam, et al., Nanoparticle-based medicines: a review of FDA-approved materials and clinical trials to date, Pharmaceut. Res. 33 (10) (2016) 2373–2387, https://doi.org/10.1007/s11095-016-1958-5.

[15] M. Rahman, Magnetic resonance imaging and iron-oxide nanoparticles in the era of personalized medicine, Nanotheranostics 7 (4) (2023) 424–449, https://doi.org/10.7150/ntno.86467.

[16] H.-V. Tran, N.M. Ngo, R. Medhi, et al., Multifunctional iron oxide magnetic nanoparticles for biomedical applications: a review, Materials 15 (2) (2022), https://doi.org/10.3390/ma15020503.

[17] Y.Q. Meng, Y.N. Shi, Y.P. Zhu, et al., Recent trends in preparation and biomedical applications of iron oxide nanoparticles, J. Nanobiotechnol. 22 (1) (2024) 24, https://doi.org/10.1186/s12951-023-02235-0.

[18] N. Wang, Y. Xie, Z. XI, et al., Hope for bone regeneration: the versatility of iron oxide nanoparticles, Front. Bioeng. Biotechnol. 10 (2022) 937803, https://doi.org/10.3389/fbioe.2022.937803.

[19] Y. Ren, J. Yang, J. Zhang, et al., Fe3O4 magnetic nanoparticles provide a novel alternative strategy for Staphylococcus aureus bone infection, Adv. Nano Res.: Int. J. (2022).

[20] V. Miguez-Pacheco, L.L. Hench, A.R. Boccaccini, Bioactive glasses beyond bone and teeth: emerging applications in contact with soft tissues, Acta Biomater. 13 (2015), https://doi.org/10.1016/j.actbio.2014.11.004.

[21] M.N. Rahaman, B.S. Bal, W. Huang, Review: emerging developments in the use of bioactive glasses for treating infected prosthetic joints, Mater. Sci. Eng., C 41 (2014) 224–231, https://doi.org/10.1016/j.msec.2014.04.055.

[22] S. Li, L. Zhang, C. Liu, et al., Spontaneous immunomodulation and regulation of angiogenesis and osteogenesis by Sr/Cu-borosilicate glass (BSG) bone cement to repair critical bone defects, Bioact. Mater. 23 (2023) 101–117, https://doi.org/10.1016/j.bioactmat.2022.10.021.

[23] H. Wang, S. Zhao, J. Zhou, et al., Biocompatibility and osteogenic capacity of borosilicate bioactive glass scaffolds loaded with Fe3O4 magnetic nanoparticles, J. Mater. Chem. B 3 (21) (2015) 4377–4387, https://doi.org/10.1039/c5tb00062a.

[24] K. Yu, B. Liang, Y. Zheng, et al., PMMA-Fe3O4 for internal mechanical support and magnetic thermal ablation of bone tumors, Theranostics 9 (14) (2019) 4192–4207, https://doi.org/10.7150/thno.34157.

[25] X. Cui, Y. Zhang, J. Wang, et al., Strontium modulates osteogenic activity of bone cement composed of bioactive borosilicate glass particles by activating Wnt/β-catenin signaling pathway, Bioact. Mater. 5 (2) (2020) 334–347, https://doi.org/10.1016/j.bioactmat.2020.02.016.

[26] T. Kokubo, H. Takadama, How useful is SBF in predicting in vivo bone bioactivity? Biomaterials 27 (15) (2006) 2907–2915.

[27] H.-T. Jiang, R. Deng, Y. Deng, et al., The role of Serpina3n in the reversal effect of ATRA on dexamethasone-inhibited osteogenic differentiation in mesenchymal stem cells, Stem Cell Res. Ther. 12 (1) (2021) 291, https://doi.org/10.1186/s13287-021-02347-0.

[28] J. Zhang, J. Jiang, H. Liu, et al., BMP9 induces osteogenic differentiation through up-regulating LGR4 via the mTORC1/Stat3 pathway in mesenchymal stem cells, Gene. Dis. 11 (3) (2024) 101075, https://doi.org/10.1016/j.gendis.2023.101075.

[29] H. Zhang, L. Li, L. Chu, et al., Dual-functional borosilicate glass (BSG) delivery implant for osteomyelitis treatment and bone regeneration, Compos. B Eng. (2023) 259, https://doi.org/10.1016/j.compositesb.2023.110749.

[30] X. Cui, Y.D. Zhang, H. Wang, et al., An injectable borate bioactive glass cement for bone repair: preparation, bioactivity and setting mechanism, J. Non-Cryst. Solids 432 (2016) 150–157, https://doi.org/10.1016/j.jnoncrysol.2015.06.001.

[31] G. Pefanis, N. Maniotis, A.-R. Tsiapla, et al., Numerical simulation of temperature variations during the application of safety protocols in magnetic particle hyperthermia, Nanomaterials 12 (3) (2022), https://doi.org/10.3390/nano12030554.

[32] E.A. Monu, M. Valladares, D.H. D'Souza, et al., Determination of the thermal inactivation kinetics of Listeria monocytogenes, Salmonella enterica, and Escherichia coli O157:H7 and non-O157 in buffer and a spinach homogenate, J. Food Protect. 78 (8) (2015) 1467–1471, https://doi.org/10.4315/0362-028X.JFP-14-488.

[33] M.E. Jacob, J. Bai, D.G. Renter, et al., Comparing real-time and conventional PCR to culture-based methods for detecting and quantifying Escherichia coli O157 in cattle feces, J. Food Protect. 77 (2) (2014) 314–319, https://doi.org/10.4315/0362-028X.JFP-13-304.

[34] I.P. Richardson, R. Sturtevant, M. Heung, et al., Hemodialysis catheter heat transfer for biofilm prevention and treatment, Am. Soc. Artif. Intern. Organs J. 62 (1) (2016) 92–99, https://doi.org/10.1097/MAT.0000000000000300.

[35] X. Xu, X. Liu, L. Tan, et al., Controlled-temperature photothermal and oxidative bacteria killing and acceleration of wound healing by polydopamine-assisted Au-hydroxyapatite nanorods, Acta Biomater. 77 (2018) 352–364, https://doi.org/10.1016/j.actbio.2018.07.030.

[36] A. O'Toole, E.B. Ricker, E. Nuxoll, Thermal mitigation of Pseudomonas aeruginosa biofilms, Biofouling 31 (8) (2015) 665–675, https://doi.org/10.1080/08927014.2015.1083985.

[37] M. Palau, E. MuñOZ, N. Larrosa, et al., Hyperthermia prevents in vitro and in vivo biofilm formation on endotracheal tubes, Microbiol. Spectr. 11 (1) (2023) e0280722, https://doi.org/10.1128/spectrum.02807-22.

[38] M. Yusefi, K. Shameli, Y.E.E.O. Su, et al., Green synthesis of Fe3O4 nanoparticles stabilized by a Garcinia mangostana fruit peel extract for hyperthermia and anticancer activities, Int. J. Nanomed. 16 (2021) 2515–2532, https://doi.org/10.2147/IJN.S284134.
[39] R. Fopase, V. Saxena, P. Seal, et al., Yttrium iron garnet for hyperthermia applications: synthesis, characterization and in-vitro analysis, Mater. Sci. Eng., C 116 (2020) 111163, https://doi.org/10.1016/j.msec.2020.111163.
[40] J. Crezee, N.A.P. Franken, A.L. Oei, Hyperthermia-based anti-cancer treatments, Cancers 13 (6) (2021), https://doi.org/10.3390/cancers13061240.
[41] W. Li, W. Wei, X. Wu, et al., The antibacterial and antibiofilm activities of mesoporous hollow Fe3O4 nanoparticles in an alternating magnetic field, Biomater. Sci. 8 (16) (2020) 4492–4507, https://doi.org/10.1039/d0bm00673d.
[42] C.H. Fang, P.I. Tsai, S.W. Huang, et al., Magnetic hyperthermia enhance the treatment efficacy of peri-implant osteomyelitis, BMC Infect. Dis. 17 (2017), https://doi.org/10.1186/s12879-017-2621-4.
[43] C.W. Chung, B.W. Liao, S.W. Huang, et al., Magnetic responsive release of nitric oxide from an MOF-derived Fe O @PLGA microsphere for the treatment of bacteria-infected cutaneous wound, ACS Appl. Mater. Interfaces 14 (5) (2022) 6343–6357, https://doi.org/10.1021/acsami.1c20802.
[44] Y. Luengo, B. Sot, G. Salas, Combining Ag and γ-Fe2O3 properties to produce effective antibacterial nanocomposites, Colloids Surf. B Biointerfaces 194 (2020) 111178, https://doi.org/10.1016/j.colsurfb.2020.111178.
[45] H.Q. Tran, H. Alam, A. Goff, et al., Multifunctional Fe O nanoparticles filled polydopamine hollow rods for antibacterial biofilm treatment, Molecules 28 (5) (2023), https://doi.org/10.3390/molecules28052325.
[46] M.H. Kim, I. Yamayoshi, S. Mathew, et al., Magnetic nanoparticle targeted hyperthermia of cutaneous infection, Ann. Biomed. Eng. 41 (3) (2013) 598–609, https://doi.org/10.1007/s10439-012-0698-x.
[47] L. Alumutairi, B. Yu, M. Filka, et al., Mild magnetic nanoparticle hyperthermia enhances the susceptibility of biofilm to antibiotics, Int. J. Hyperther. 37 (1) (2020) 66–75, https://doi.org/10.1080/02656736.2019.1707886.
[48] L.A. Almutairi, B. Yu, E. Dyne, et al., Mild magnetic hyperthermia is synergistic with an antibiotic treatment against dual species biofilms consisting of and by enhancing metabolic activity, Int. J. Hyperther. 40 (1) (2023), https://doi.org/10.1080/02656736.2023.2226845.
[49] J. Josse, F. Valour, Y. Maali, et al., Interaction between staphylococcal biofilm and bone: how does the presence of biofilm promote prosthesis loosening? Front. Microbiol. 10 (2019) 1602, https://doi.org/10.3389/fmicb.2019.01602.
[50] W. Huang, D.E. Day, K. Kittiratanapiboon, et al., Kinetics and mechanisms of the conversion of silicate (45S5), borate, and borosilicate glasses to hydroxyapatite in dilute phosphate solutions, J. Mater. Sci. Mater. Med. 17 (7) (2006) 583–596.
[51] P. Tian, L. Zhao, J. Kim, et al., Dual stimulus responsive borosilicate glass (BSG) scaffolds promote diabetic alveolar bone defectsrepair by modulating macrophage phenotype, Bioact. Mater. 26 (2023) 231–248, https://doi.org/10.1016/j.bioactmat.2023.02.023.
[52] J.T. A, C.W. G, D.W. A, et al., Tailoring Time-Varying Alkaline Microenvironment on Titanium for Sequential Anti-infection and Osseointegration [J], 2021.
[53] G.N.B.D. Reis, G.T. Cuba, W.H.D.E.C. Targa, et al., S53P4 bioactive GLASS putty in the local treatment of cavitary chronic osteomyelitis, Acta Ortopédica Bras. 31 (1) (2023) e258453, https://doi.org/10.1590/1413-785220233101e258453.
[54] N.C. Lindfors, P. HyvöNEN, M. NyyssöNEN, et al., Bioactive glass S53P4 as bone graft substitute in treatment of osteomyelitis, Bone 47 (2) (2010) 212–218, https://doi.org/10.1016/j.bone.2010.05.030.
[55] T. Al Malat, M. Glombitza, J. Dahmen, et al., The use of bioactive glass S53P4 as bone graft substitute in the treatment of chronic osteomyelitis and infected non-unions - a retrospective study of 50 patients, Zeitschrift Fur Orthopadie Und Unfallchirurgie 156 (2) (2018) 152–159, https://doi.org/10.1055/s-0043-124377.
[56] M. Bigoni, M. Turati, N. Zanchi, et al., Clinical applications of Bioactive glass S53P4 in bone infections: a systematic review, Eur. Rev. Med. Pharmacol. Sci. 23 (2019) 240–251.
[57] M.G. Moreno, M.E. Butini, E.M. Maiolo, et al., Antimicrobial activity of bioactive glass S53P4 against representative microorganisms causing osteomyelitis - real-time assessment by isothermal microcalorimetry, Colloids Surf. B Biointerfaces 189 (2020), https://doi.org/10.1016/j.colsurfb.2020.110853.
[58] D.M. Marques, V.D. Oliveira, M.T. Souza, et al., Biomaterials for orthopedics: anti-biofilm activity of a new bioactive glass coating on titanium implants, Biofouling 36 (2) (2020) 234–244, https://doi.org/10.1080/08927014.2020.1755842.
[59] J. ZúñIGA-Miranda, J. Guerra, A. Mueller, et al., Iron oxide nanoparticles: green synthesis and their antimicrobial activity, Nanomaterials 13 (22) (2023), https://doi.org/10.3390/nano13222919.
[60] S.V. Gudkov, D.E. Burmistrov, D.A. Serov, et al., Do iron oxide nanoparticles have significant antibacterial properties? Antibiotics 10 (7) (2021) https://doi.org/10.3390/antibiotics10070884.
[61] C. Chen, L. Chen, Y. Yi, et al., Killing of Staphylococcus aureus via magnetic hyperthermia mediated by magnetotactic bacteria, Appl. Environ. Microbiol. 82 (7) (2016) 2219–2226, https://doi.org/10.1128/AEM.04103-15.
[62] N. Padmavathy, R. Vijayaraghavan, Enhanced bioactivity of ZnO nanoparticles-an antimicrobial study, Sci. Technol. Adv. Mater. 9 (3) (2008) 035004.
[63] G.R. Rudramurthy, M.K. Swamy, U.R. Sinniah, et al., Nanoparticles: alternatives against drug-resistant pathogenic microbes, Molecules 21 (7) (2016), https://doi.org/10.3390/molecules21070836.
[64] M. Salehiabar, H. Nosrati, S. Davaran, et al., Facile synthesis and characterization of L-aspartic acid coated iron oxide magnetic nanoparticles (IONPs) for biomedical applications, Drug Research 68 (5) (2018) 280–285, https://doi.org/10.1055/s-0043-120197.
[65] H.E. Daldrup-Link, Ten things you might not know about iron oxide nanoparticles, Radiology 284 (3) (2017) 616–629, https://doi.org/10.1148/radiol.2017162759.